DESIGN AND MODELING OF ADVANCED GYROSCOPES

by

Mrigank Sharma

B.E, Anna University, 2006

A THESIS SUBMITTED IN PARTIAL FULFILMENT OF
THE REQUIREMENTS FOR THE DEGREE OF

Master of Applied Science

in

The Faculty of Graduate Studies

(Electrical and Computer Engineering)

The University of British Columbia

(Vancouver)

September, 2008

Abstract

This thesis reports on a design and modeling of a micro-machined gyroscope. The proposed sensor is a dual mass type, electro-statically driven to primary mode oscillation and senses, capacitively, the output signal. Full decoupling between drive and sense modes minimizes the mechanical crosstalk and based on this a novel gyroscope is designed and modeled which has separate sensing and driving masses. The dual mass gyroscope is designed such that driving and sensing resonant frequency is 23101 Hz with 0% mismatch (in simulation)with quality factor of 31.6227 and bandwidth of 730.51Hz. The gyroscope when actuated in simulation with 25V ac and 10V dc showed sensing capacitance variation of 126aF for 1 rad/s with base capacitance of 244.16fF. To the design of the gyroscope a new semi automatic tool was formulated for the noise analysis and noise based optimization of the resonant MEMS structures. Design of a sensitive gyroscope needs to take into account the noise shaping induced by damping phenomena at micro scale and is critical for optimization. The analysis was further extended to the design of the gyroscope and estimation shows that there is a trade off between the S/N ratio and the sensitivity and the design could be made much better in-terms of S/N by tuning its resonant frequency to 10^6Hz.

Table of Contents

List of Tables

List of Figures

Acknowledgements

My sincere gratification to the blessings and love of my parents and brother to whom I owe everything what little I have achieved so far. I whole heartily thank Professor Edmond Cretu for his constant guidance, patience and financial support for my graduate studies, Professor N.Venkateswaran for introducing me into the wonderful world of research during my undergraduate years. My acknowledgement would not be complete without mentioning names of Miguel Angel Guillen Torres of Dr.Lukas Chrostowski's lab and Farid Ullah Khan of Dr.Mu chiao's lab for helping me with the experimental setup. I also would like to acknowledge my friends especially Akila Kannan, Vijayalakshmi Sridhar and Chaitanaya here at Vancouver for always being there for me.

I dedicate my thesis to illusion (Mother Maya).To "Hope" that there would be a better tomorrow for me and you and people around us.

Chapter 1

Introduction

Micro electromechanical systems (MEMS) are changing the way we live in many areas such as entertainment, aviation, navigation and in many many more areas. Angular rate sensors (gyroscope) have been effectively implemented in navigation especially in automotive, aerospace and military applications and this paves us to explore the avenues in minimally invasive surgery (MIS). In Appendix A of the thesis a review on MIS is carried out and is observed that very high sensitivity is required for the navigation of tools. Hence, this thesis is written to understand, design and model a sensitive angular rate sensor which could be a part of arrays of inertial sensors aiding doctors in navigation.

The structure of the thesis is such that in the first chapter the motivation is defined, in the second chapter the concept of a 2-DOF gyroscope is presented ,chapter 3 discusses the different aspects of gyroscopes from the structure to design issues. Chapter 4 discusses the concept of dual mass gyroscope, chapter 5 the implementation of the gyroscope using the SOIMUMPS technology ,chapter 6 talks about the experimental verification and finally the chapter 7 discusses the concept of noise analysis and noise optimization of gyroscope. To sum up the structure of this thesis, it defines a problem and discusses alternative methods to fine tune the final structure of the gyroscope.

1.1 Microgyroscope And Their Applications

Plenty of literature is available on the design of gyroscopes and most of it based on the concept of Coriolis force being generated and sensed by the mechanical part. The concept of utilizing the vibrating elements to induce and detect Coriolis force involving no rotating parts (requiring bearings) has proven to be very effective. The proof mass is generally suspended above the substrate by a suspension system consisting of flexible beams. The overall dynamical system is typically a two degrees-of freedom (2-DOF) mass-spring-damper system, where the rotation-induced Coriolis force causes energy transfer to the sense-mode proportional to the angular rate input. In most of the reported micro-machined vibratory rate gyroscopes, the proof mass is driven into resonance in the drive direction by an external sinusoidal electrostatic or electromagnetic force. When the gyroscope is subjected to an angular rotation, a sinusoidal Coriolis force is induced in the direction orthogonal to the drive-mode oscillation at the driving frequency. Usually the resonant frequency of the drive mode and the sense mode is desired to be same to get the high sensitive device. However there are work which have showed small shift in the resonant frequencies to get high bandwidth[2]. There is always a tradeoff between the the bandwidth and the sensitivity and it is up to the designer to tune the gyroscope in accordance with the need. With the advent of technology capabilities smaller, cheaper, lighter gyroscopes can be made available

with electronics and mechanical structure on the same substrate. The gyroscopes have wide applications in navigation systems, aerospace, military, consumer electronics and medical applications. The GPS system, missile launching, helicopter navigation, camcoder image stabilization etc ,all use gyroscope. Figure 1.1 shows some of the industrial gyroscopes which are used in the automobile and photography.

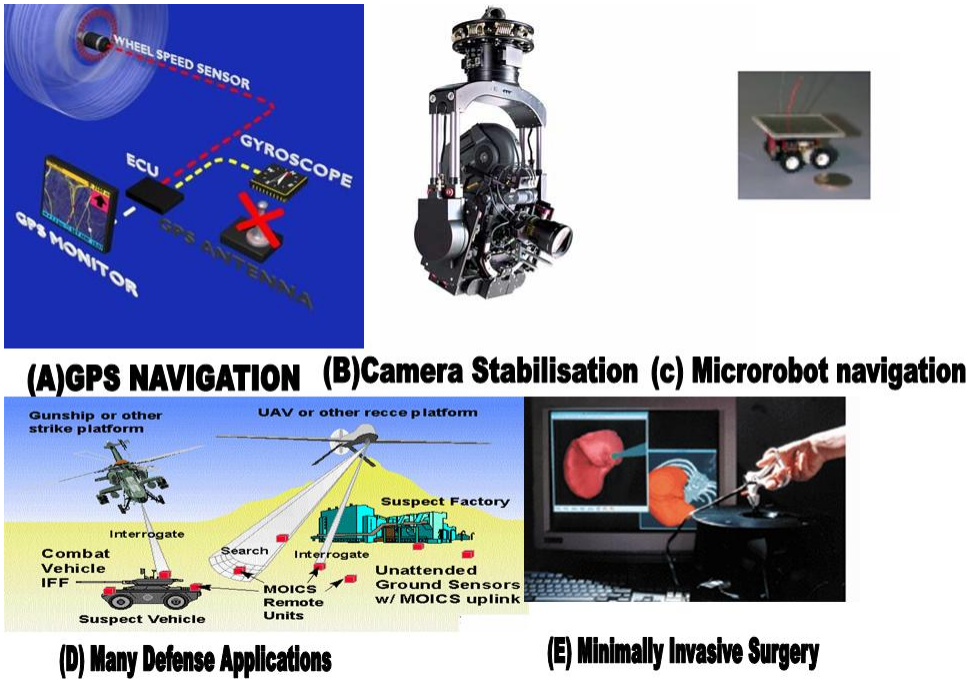

Figure 1.1: MEMS Applications(A[20],D[21], E[22])

1.2 Research Motivation

Computer Aided Surgery is becoming popular as it improves the performance of the doctors who are constantly being aided by the computer. In the past (not far) the patient had to be cut open to perform any kind of surgery, this leading to more pain for the patients and increase in time and reduction of efficiency. Among the clear benefits expected from MEMS technology one can mention: improve surgical outcome, lower risk, lower treatment and post-surgery costs, shorter recovery periods and decrease in patient trauma. Medical navigation systems are mainly used for monitoring the position of surgical instruments relative to patient body. Some optical navigation systems have presently a limited applicability (e.g. in neurosurgery), but their use is hindered by the high cost and the need of a dire. The MEMS-based unit will comprise accelerometers as well as gyroscopes, together with associated electronics. Surgical applications of an increased complexity will benefit from an enhanced 3D position, e.g. bone repositioning in case of facial fractures and osteotomies of

craniofacial segments. One of the main goals is to improve the resolution and accuracy of the present MEMS-based inertial sensors and exploit their potential in Computer Assisted Surgery (CAS). The presently available resolutions of (commercial) MEMS sensors are in the range of mg for accelerometers, and around 0.1deg/sec for gyroscopes. Advanced medical navigation systems require sensing linear accelerations in the micro-g or lower ranges, and angular rates around 0.01deg/sec or better. As the size is scaling down the inertial mass also scales down thus limiting the sensing capability. Another issue is the cross-coupling of modes while sensing, the design should be robust and should have decoupling in different directions. This thesis would mainly focus on the design of the gyroscope keeping all these issues in mind.

1.3 Objectives And Methods

The motivation of this research is to design and model a high sensitive gyroscope. This gyroscope along with the accelerometer would be a part of the navigation system. In 1.2,the block diagram depicts that there is a software in which the movement of tool is predefined in terms of co-ordinates. When a tool like a catheter is actually inserted in the body through a keyhole, its movement is tracked and matched against the coordinates of a software map. The minimal inertial sensors both accelerometers and gyroscopes are used for linear and rotational movement. Both these structures have interdigited plates acting like capacitors. These capacitors vary with the linear motion in case of accelerometer and with the rotational motion in gyroscopes, thus varying the distance between the interdigited plates. The net capacitances can be evaluated and so the voltages associated too.

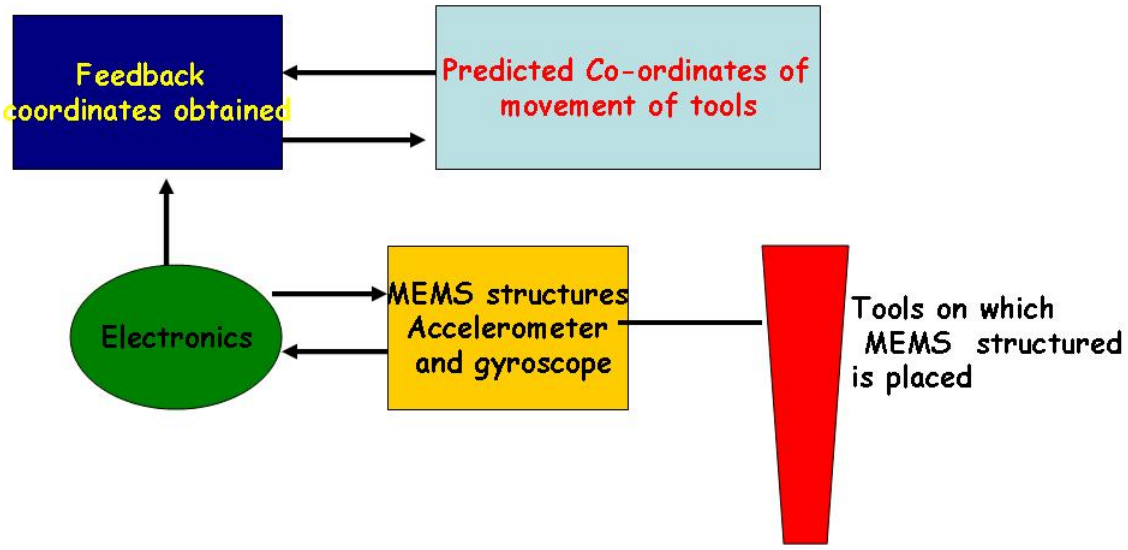

Figure 1.2: Block Diagram of The Futuristic Navigation Using Gyroscope in Minimally Invasive Surgery

This gyroscope which could be used in the MIS uses the methodology of dual mass sensing and the sensitivity is dependent on the stiffness and mass ratio of the outer masses. Each external mass(secondary) is suspended by two beams with the inner mass and resonates at $\omega = \sqrt{k/m}$. The k/m ratio can be tuned to achieve different resonant modes or matched resonant mode with the inner mass. There are nevertheless many articles on gyroscope with high sensitivity using single mass but doesn't solve the problem of cross-coupling. There are also papers with differential gyro concept but they cater to the need of high bandwidth and low sensitivity. There are also gyroscope which sense rotation in the Z-direction and have proved that the capacitive sensitivity increases but not many technologies offer out-off plane capacitive sensing. This thesis caters to all issues relates with the dual mass gyroscope and shows the evolution of the finalized structure.

1.4 Prior Work On Microgyroscopes

Although there are numerous research groups all around the world working on the gyroscope, I would be highlighting only the significant moments. Draper Laboratory reported the first micro-machined gyroscope in 1991, utilizing a double-gimbal single crystal silicon structure suspended by torsional flexures; and demonstrated 40°/s/pHz resolution at 60Hz bandwidth [1].Since then many changes have happened with the continuous change in technology/processes etc. The research work at UC Irvine of Cenk Acar is very close conceptually. In [2], there is increase of DOF(Degree of freedom) by increasing the number of masses, their research focusses on low sensitivity and operate at frequency range where the sensitivity is minimum to create a robust system for applications like aerospace. Dr. Tayfun's group[3] came up with the high performance SOI MEMS gyroscope which operates at the atmospheric pressure and has decoupled modes of oscillations. This work is interesting as they used SOIMUMPS technology as used by us for fabrication. MLX90609 , gyroscope by the MELEXIS has a sensitivity of 0.0027°/s [4] which uses optimized analog pre-amplifiers and a Digital Signal Processing (dsp) for the signal treatment. The general specification of gyroscopes is given by Scale factor and Zero-rate output(ZRO). Scale factor is given as amount of change in output per unit change rotation [V/(°/s)]. Zero-rate output (ZRO)is given as the change in output in the absence of angular rate, its the sum of white noise and a slowly varying function (noise defines resolution $[(°/s)/\sqrt{Hz}]$)and slowly varying function defines drift [°/s]

Chapter 2

Concept of Single Mass Gyroscope

2.1 Dynamics of Resonating Gyroscope

The concept of the gyroscope can be best understood by the free body diagram. A single mass has 2 DOF(degree of freedom) and can move in X and Y direction. A gyroscopic effect can be seen when a Coriolis force acts upon the mass in a rotational frame and hence looks as if it is tilting the mass. As seen in the Figure 2.1, a gyroscope can be visualized

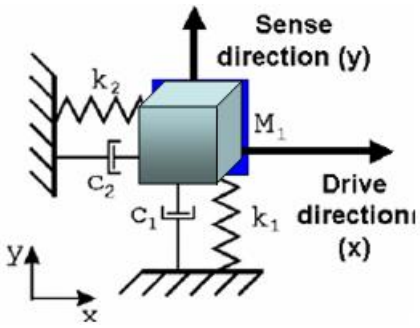

Figure 2.1: Free Body Diagram of a Single Mass

as a mass suspended by springs and dampers in each direction(sense and driving). The dynamics of the gyroscope is defined by the tuning of dampers and spring with the mass. Most of the gyroscopes reported have single mass suspended over the substrate with 2 sets of comb drives and 2 sets of flexures. The accelerations experienced by a moving body in a rotating reference frame can be obtained and is presented in [2]

The term $2m\overrightarrow{v} \times \overrightarrow{\Omega}$ is of importance and is the Coriolis force. Here v is the velocity(m/s) of mass m and Ω(rad/s) is angular velocity. The 2DOF mass has two directions sense and driving and hence the oscillations in these two directions are considered.

$$m\ddot{x} + c_x\dot{x} + k_x x = 2m\Omega_z\dot{y} \qquad (2.1)$$

$m\ddot{y} + c_y\dot{y} + k_y y$ =-2m$\Omega_z\dot{x}$ (2.2)

The right hand side of eq(2.1) and (2.2) have the Coriolis force acting on each system. In both equations the Ω is in the z direction ,which is perpendicular to both x and y as shown in the free body diagram. This can be further simplified in terms of terms as $\omega_x = \sqrt{k_x/m}$ and $\omega_y = \sqrt{k_y/m}$ These two modes can be matched by tuning the stiffness constant and the mass.

2.2 Coriolis Response

A simple gyroscope is shown in the figure 3.1.Here a mass is suspended with crab leg flexures. Here the mass is forced into oscillations in the x-direction(drive)mode. When a Coriolis force $2m\overrightarrow{v_B} \times \overrightarrow{\Omega}$ acts on this mass ,it induces a motion in y-direction (sense). The angular rate is then computed by obtaining the capacitance variation in y direction. Coriolis force is always in 90 degree phase difference to both the drive and sense mode. This is further seen for the gyroscope shown in the 2.2

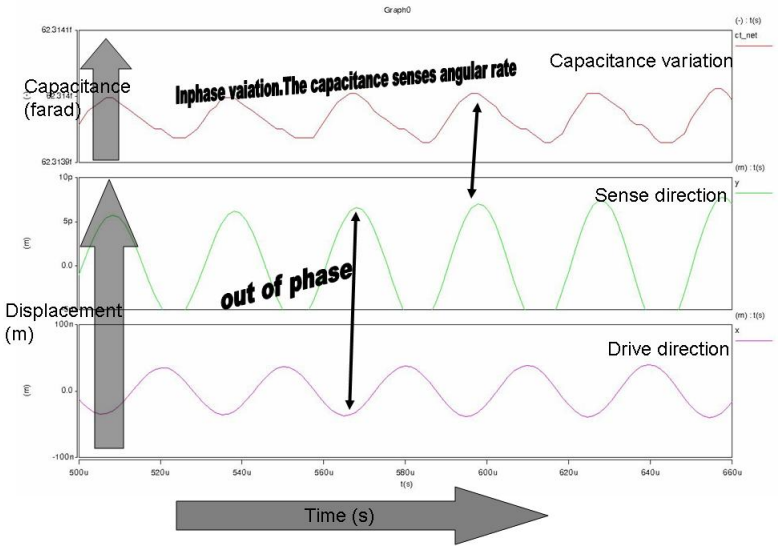

Figure 2.2: Coriolis Response Observed In Coventorware for 2DOF

2.3 Frequency Response and Operation

To achieve maximum possible gain, conventional gyroscopes are generally designed to operate at or near the peak of the response curve. This is typically achieved by matching drive and sense resonant frequencies. However, the system becomes very sensitive to variations in system parameters causing a shift in the resonant frequency. There are also gyroscopes with initial mismatch in the modes to get higher bandwidth and lower sensitivity. The Figure 2.3 shows that there is difference of 1231Hz in the sense and driving of the gyroscope. The capacitance variation is sensitive in the y direction as shown in the top of the figure 2.3.

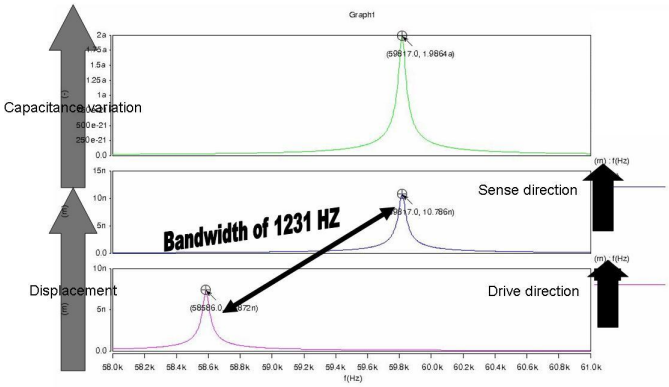

Figure 2.3: The Mismatch in the Drive and Sense Mode of Operation.This Increases the Bandwidth and Decreases the sensitivity

To get a high sensitivity the design is tuned to $\omega_x = \sqrt{k_x/m}$ and $\omega_y = \sqrt{k_y/m}(\omega_x = \omega y)$, such that the drive and sense modes have matching resonant frequencies. The figure 2.4 shows that both the sense and drive are at same frequency. Damping also affects the sensitivity as Q is inversely proportional to damping as given as $Q = \sqrt{km}/b$ (where Q is quality factor,k is stiffness constant and b is the damping coefficient).

The masses usually have holes etched out of them to release the structure from the silicon substrate. This aids in the fabrication process but affects the sensitivity as it is inversely proportional to the square root of mass as seen by the previous equations.The gyroscope has to be tuned for its operation so that it is not overdamped. The normal operation of the gyroscope is near the area of high sensitivity. However damping reduces the sensitivity as seen in the figure 2.3(here when Q is high frequency response is sharper when low,response is wider).Therefore there is tradeoff between the sensitivity and the bandwidth.

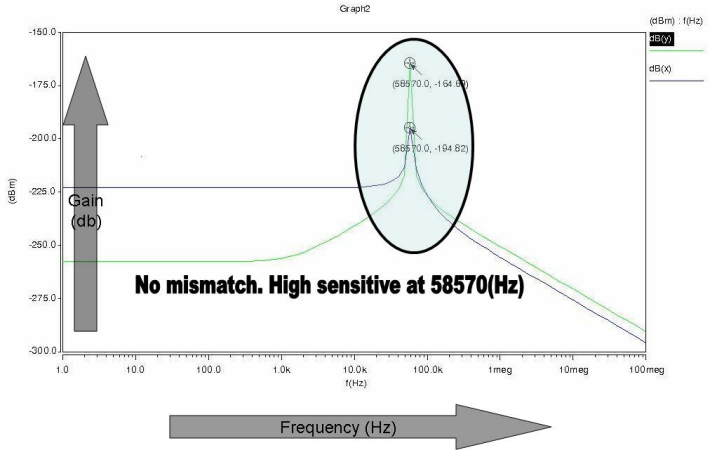

Figure 2.4: No Mismatch in the Drive and Sense Mode of Operation.High Sensitivity at 58570 Hz

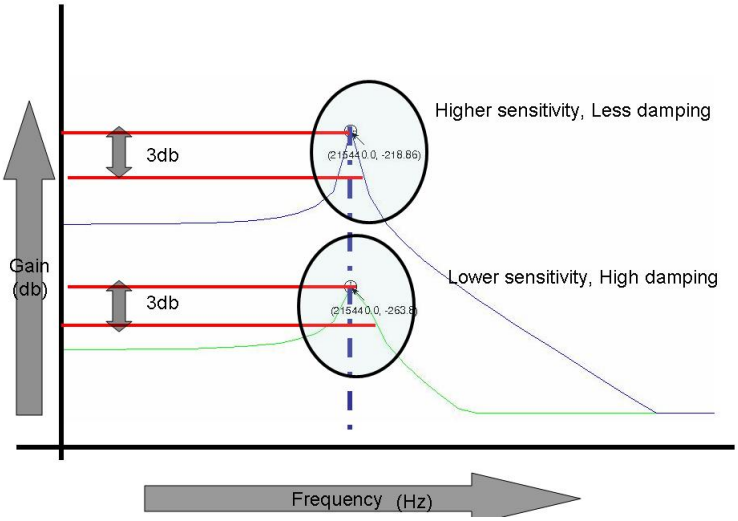

[Damped/Underdamped Operation]Comparision of Damped and Underdamped system

Chapter 3

Basics of MEMS Gyroscope Structure

3.1 Introduction

3.2 Mechanical Design

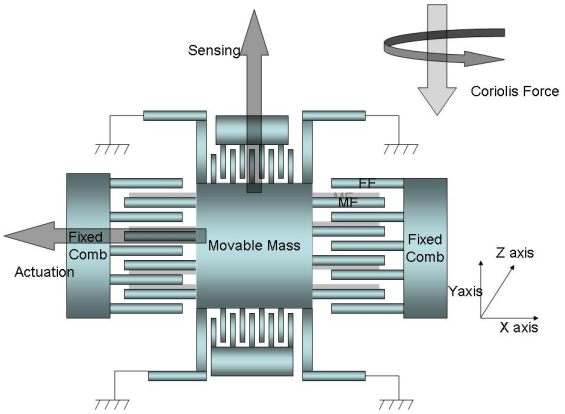

Figure 3.1: The Diagram of a Typical 2-DOF Gyroscope with Capacitive Readout

The micro-gyroscope structure shows the suspended mass with four crab leg flexures. There are also comb drives(set of parallel plates) for sensing and driving the micro-gyroscope. In figure 3.1a simple concept of gyroscope is illustrated where the actuation takes place in the x direction .When angular rate is applied along the Z-axis ,Coriolis force is induced and sensing happens in the y direction. The designer should also decide upon the technology for machining the gyroscope. Technologies like SOIMUMPS allow back etching to release the structure and hence the perforations on the suspended mass is not required. This works for the benefit of the designer as higher mass means higher sensitivity.The designer can tune various parameters like damping(operation of frequency),stiffness constants and mass in the design stage in order to achieve the desired performance as seen in figure 3.2. Figure 3.2 shows damping force as a resistive force which contributes to mechano-thermal noise.

As the damping is frequency dependent, tuning of the suspensions should be done such that the gyroscope operates at the local minima of the damping. This concept of noise due to damping is extensively elaborated in the forthcoming chapters. The next subsections

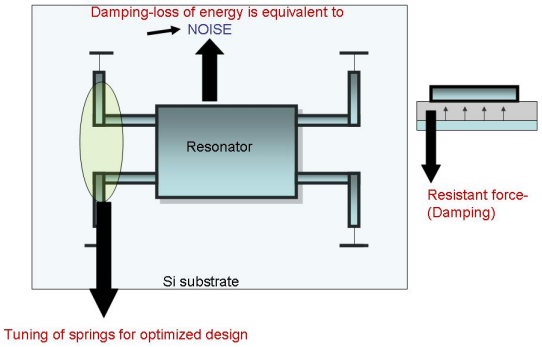

Figure 3.2: Tuning of Parameters for a Gyroscope Design

would address the design of the different parts of the gyroscope.

3.2.1 Suspension System Design

Design of the suspensions is crucial as almost all existing micro machined vibratory gyroscopes operate on the principle of detecting the sinusoidal Coriolis force induced on a vibrating proof-mass in the presence of an angular-rate input. As the induced Coriolis force is orthogonal to the drive-mode vibration, the proof-mass is required to be free to oscillate in two orthogonal axes.The resonant MEMS structures usually have a mass suspended over the substrate using the elastic flexures. There are many flexures reported like straight beam,crab-leg,u-shape and others as shown in3.3.

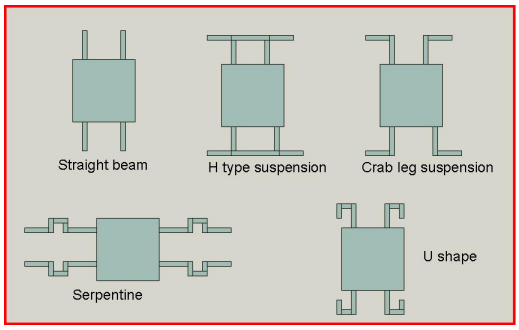

Figure 3.3: Different Suspensions

To understand the modeling of the different beam flexures a simple example of straight beam is studied as seen in figure 3.4 here three parameters define the stiffness of the flexure namely(width,length and the thickness)

The translation stiffness for the beam loaded at one end is the ratio of the force and the deflection of the beam due to the force. It can be theoretically expressed as $Kstiffness = Etw^3/L^3$ where E is Young's modulus ,t is thickness ,l is length and w is width. Now

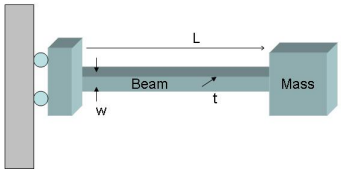

Figure 3.4: Straight Beam Under Translation Deflection

assuming that these beams are suspending the mass , the net stiffness constant would be computed as the sum of four independent stiffness of flexures $4 \times Etw^3/L^3$ .The bent u-shape flexure , two fixed-guided beams deform translationally in series, and four of these double-folded flexure define the overall stiffness $4/2 \times Etw^3/l^3$. The other most popular flexure is crab leg and looks like as shown in figure 3.5

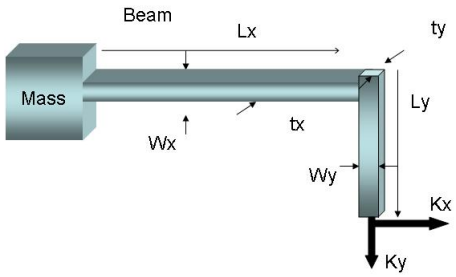

Figure 3.5: Crab Leg Flexure With One End Loaded

The crab leg suspension has two beams x and y ,in our case the beam y is loaded as seen in Figure 3.5. In this case the stiffness in the y direction is very high and the stiffness in the x direction comparatively less, so that mass could resonate in the x direction. According to [6] the stiffness coefficients are

$$K_x = E \times t \times w_x^3 \times (l_x + 4 \times l_y)/{l_x}^3 \times (l_x + l_y) \qquad (3.1)$$

$$K_y = E \times t \times w_y^3 \times (l_y + 4 \times l_x)/{l_y}^3 \times (l_y + l_x) \qquad (3.2)$$

While designing the suspensions , the dependance of the stiffness constant with the length and width variation can give insight to choose the appropriate dimension. An analysis is carried out by keeping the dimensions of one beam of the crableg constant and by varying the width and length of the other in SOIMUMPS technology. The graph was plotted in MATLAB , with length as x axis and K stiffness as Y axis. The graph showed a polynomial dependance between stiffness and length. The plot as seen in Figure 3.7show that the K Vs L follows polynomial (degree 3 variation) and also validates equations.

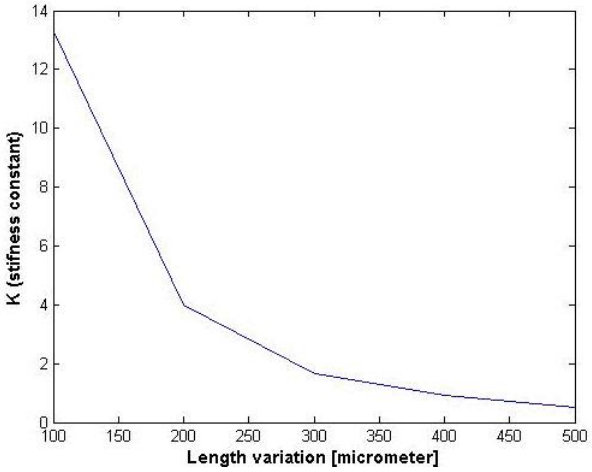

Figure 3.6: Stiffness Variation with Length Variation

Similar analysis is carried out for the width variation with respect to stiffness constant keeping constant length 3.8 The graph in 3.8 is nonlinear initially and then seems linear after the width 10um. The reason for this could be the range of data which is small (5 to 20um). The 3.9 and 3.10 show the curve fitting to prove the nonlinearity of the system.

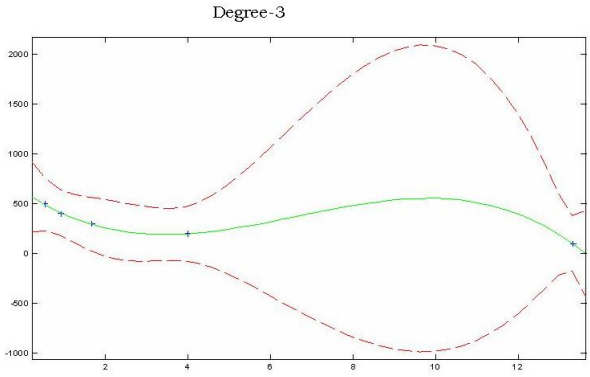

Figure 3.7: Polynomial Fit to the Curve (Degree 3 ,The Green Line Follows the Points.

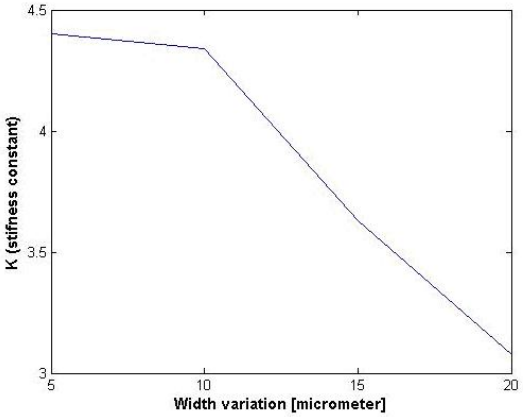

Figure 3.8: Stiffness Variation with Width Variation

As the curve here shows that the width variation is not linear , the polynomial fit is carried out with the second order fit and is seen in 3.10

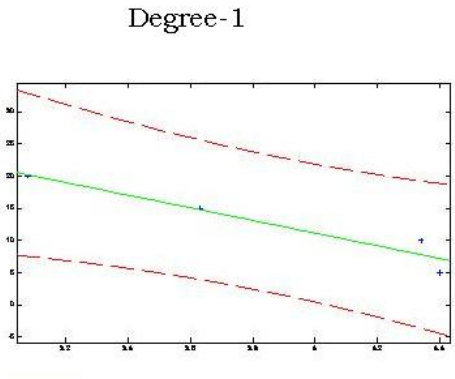

Figure 3.9: Linear fit (Green Line does not Follow the Points)

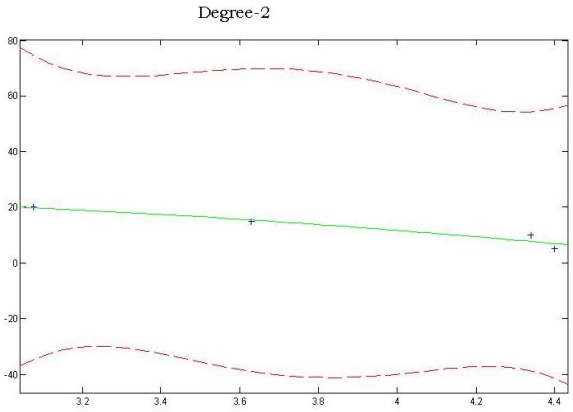

Figure 3.10: Polynomial Fit (Degree 2) ,Green Line Follows the Point Closely

3.2.2 Damping Estimation

The major damping mechanism in the gyroscope structure is the viscous effects of the air surrounding the vibratory structure, and confined between the proof mass surfaces and the stationary surfaces as these sensitive resonating structures have suspended masses which encapsulate gases or liquids underneath them and operate at large frequency range. The damping of the structural material is usually orders of magnitude lower than the viscous damping, and is generally neglected. The resulting damping in the gyroscope dynamical system is dominated by the internal friction of the air between the proof-mass and the substrate, and between the comb-drive and sense capacitor fingers. The damping can be broadly classified as slide film and squeeze film. According to [7] slidefilm damping is not as significant as the squeeze film . In 3.11 shows the significance of different damping. The slide film damping coefficient could be computed as

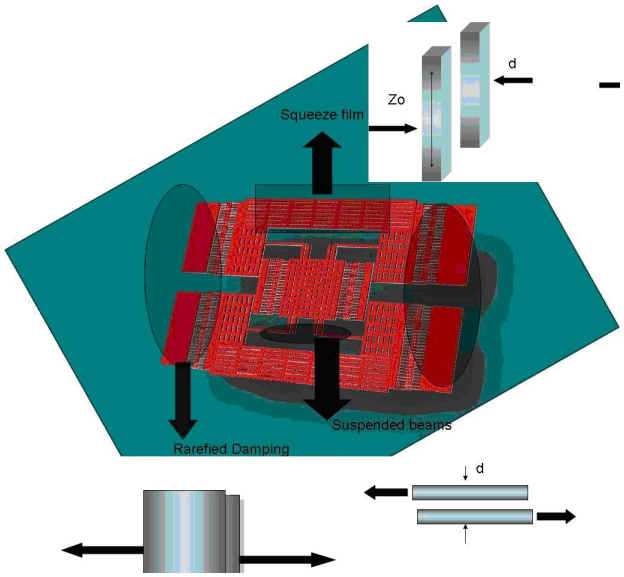

Figure 3.11: Damping In a Gyroscope

$$C_{slidefilm} = \mu PA/d_0 \qquad (3.1.1)$$

Here μ is the viscosity ,P is the pressure ,A is the area between the plates and d_0 is the distance between them as seen in figure 3.12

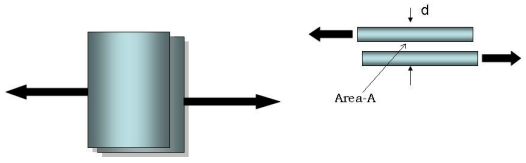

Figure 3.12: Slide Film Damping

Similarly for the squeeze film damping

$$C_{squeeze} = \mu \times 7 \times PZ_0A/d_0^2 \quad (3.1.2)$$

Here μ is the viscosity ,P is the pressure ,A is the area between the plates and d_0 is the distance between them ,$Z_0$is the length of the plates under which the air gets encapsulated as seen in figure 3.13

There are many papers [7] [8] [9] [17][18]on the analytical modeling of the damping. The squeeze film damping force can be computed as

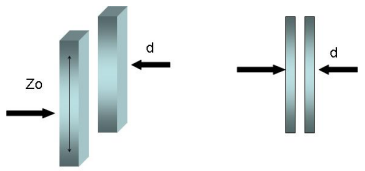

Figure 3.13: Squeeze Film Damping

$$F_d = 64\sigma PA/\Pi^6 h \sum_{m,nodd} m^2 + (n/\beta)^2/(mn)^2[m^2 + (n/\beta)^2) + \sigma^2/\pi^4] \quad (3.1.3)\ [9]$$

Here A is the area of the movable rectangular plate, of length L and width W, β is L/W, h is the displacement,η is effective viscosity and $\sigma$is the squeeze number.

The across and through representation as seen in 3.14 models the resonator system. First two branches represent the mass and the stiffness of the system and the parallel branches with resistor and inductors in series represent the damping. The value of the resistors sets the magnitude of the noise and the inductor shapes the noise induces by damping. The selection of three branches is done as the higher order of branches would be less significant as the value of lowest resistor would be significant in the parallel representation. The value of resistors and inductors could be got by theory [9] as

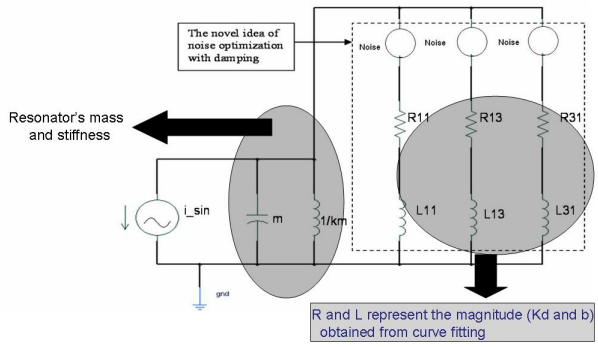

Figure 3.14: Across and Through Model of Damping Representation

$$B_{mn} = 786\eta/\Pi^6 {h_0}^3 \times (mn)^2(m^2/w^2 + n^2/l^2)\ (3.1.4)\ [9]$$

$$K_{mn} = 64AP/\Pi^4 h(mn)^2\ (3.1.5)\ [9]$$

here m and n are the odd numbers,$\eta$is the ambient viscosity, A is the area ,w is the width of the plate,h is the displacement causing the damping. Equations (3.1.4) and (3.1.5) is solved for m=0,n=0 and R11 can be approximated as $2/b_{00}$, $L11$ as $1/k_{00}$,R13 as $90/b_{00}$,L13 as $9/b_{00}$. To illustrate the dominance of the resistance on the magnitude of damping,

noise analysis using the Nyquist formula is carried out ,which uses $\sqrt{4KTb}$ where K is the Boltzman's constant,T is the temperature and b is the damping. In 3.15 the spectral noise density corresponding to resistance obtained from the (3.4) and (3.5). The noise due to damping at higher frequency reduces as seen in 3.15

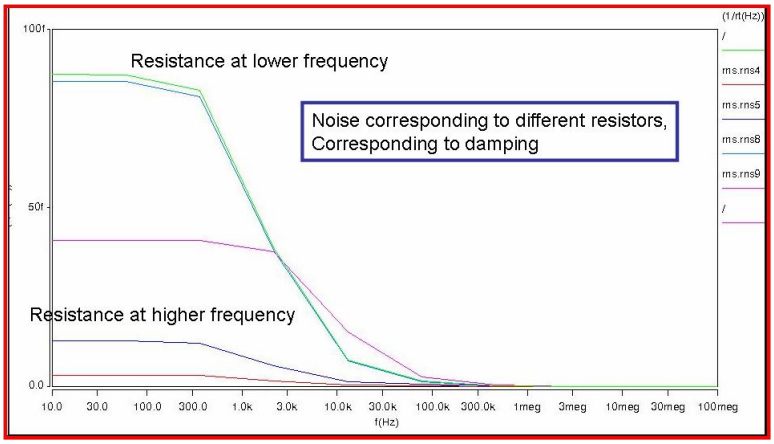

Figure 3.15: Variation of Nyquist Noise (Damping)with Frequency

3.3 Electrical Design

The actuation and sensing of the resonant system 3.16 usually considers electrostatic methods due to their ease of fabrication,integration, good DC response,noise performance , high sensitivity and low temperature sensitivity [11][12]. The actuation and sensing in the mechano-electrical domain can be modeled with parallel plate capacitors with movable plates. The capacitance between the parallel plate capacitor can be evaluated by the formula Area overlap$\times\epsilon$/distance of separation between the plates. $Capacitance = A\epsilon/d^2$ were ϵ is the dielectric constant, A is the area overlap and d is the distance between fixed and movable plates.

3.3.1 Electrostatic Actuation

Interdigitated comb-drives(set of parallel plate capacitors)are one of the most common actuation structures used in MEMS devices [2][10]. Linearized drive forces along the x-axis can be achieved by appropriate selection of voltages applied to the opposing comb-drive sets. Actuation is done by applying $V_1 = V_{DC}+V_{AC}$to one set of comb drives, and $V_2 = V_{DC}-V_{AC}$ to the other set, where $V_{DC}$is a constant bias voltage, and V_{AC}as seen in 3.17 is a time-varying voltage. Assuming negligible deflections along the y-axis, the net electrostatic force reduces to

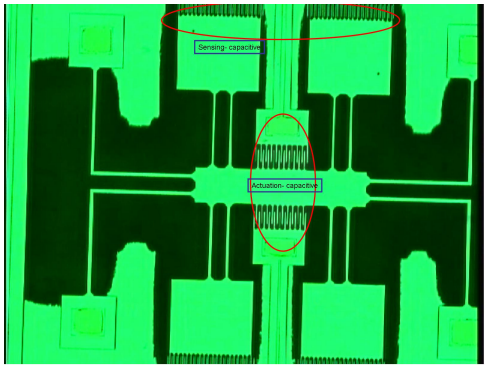

Figure 3.16: Actuation and Sensing-Capacitive

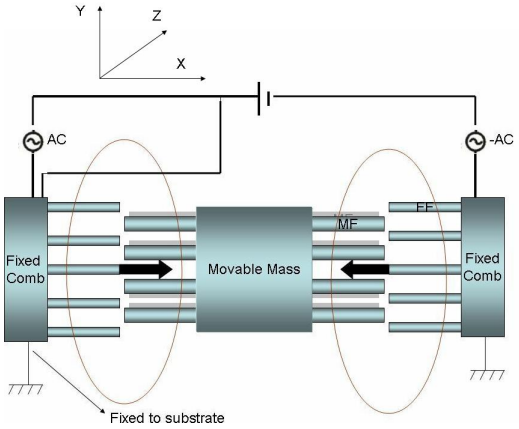

Figure 3.17: Electrostatic Actuation

$$F_{actuation} = -U(potentialenergy) = \nabla C(x,y,z)V^2/2 = N(\epsilon_0 z)V^2/2y \quad (3.2.1)$$

Here $\epsilon$is the permittivity,z is width of the finger, N is number of fingers and y is the separation of the fingers.

3.3.2 Capacitive Detection

Sensing is a differential pair of gap varying capacitors as seen in 3.18

When the mass resonates, the fingers move up and down resulting in capacitance variation. Due to the movement of the fingers capacitances can be modeled as

$$C_{sense+} = \epsilon \times t \times l \times N/(y + y_0) \quad (3.2.2)$$

$$C_{sense-} = \epsilon \times t \times l \times N/(y - y_0) \quad (3.2.3)$$

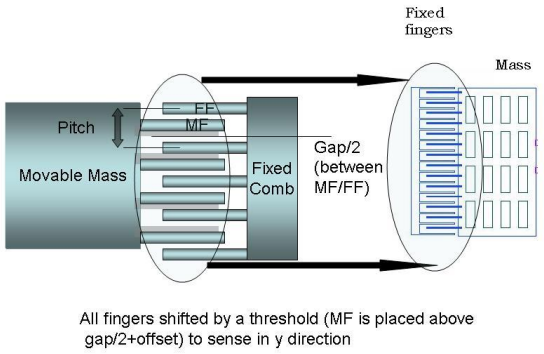

Figure 3.18: Capacitive Sensing

Here $C_{sense+}$is capacitance variation when the movable finger moves closer to fixed finger and$C_{sense-}$is capacitance variation when movable finger moves away from fixed finger as seen in 3.19 Hence the net capacitance would be the sum of

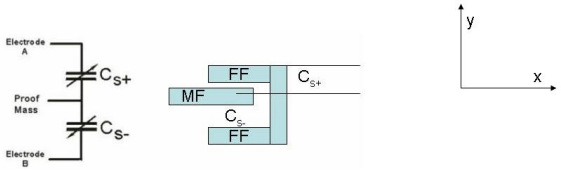

Figure 3.19: Capacitive Sensing

$$\triangle C = C_{sense+} - C_{sense-} \qquad (3.2.4)$$

$$\triangle C = 2 \times \epsilon \times t \times l \times N/y^2 \qquad (3.2.5)$$

3.3.3 Influence of Parameters on Sensitivity

Gyroscopes can be defined by the following specifications as shown in Table1

ω_x	$\sqrt{k_x/m}$
ω_y	$\sqrt{k_y/m}$
Quality Factor(Q_y)	$\sqrt{k_y \times m}/b_y$
$Sensitivity(y/\Omega)$	$(2 \text{ m} \times\omega_x \times \omega_y \times F_d)/k_x k_y$
$Bandwidth$	f_0/Q or $1/(2\pi) \times (\omega)/Q$

Parameters of Gyroscope[24]

To achieve the high sensitivity the movable mass needs to be designed should be as large as possible as seen in the Table1. The stiffness of the resonator should be adjusted accordingly to design the structure to operate at required frequency($\omega = \sqrt{k/m}$). Damping is dependent on the frequency and would contribute to the elasto-damping noise. The impact of the squeeze film damping is highest at the low frequency and reduces as the frequency increases[14][15]. The sensitivity on the other hand is higher in the low frequency domain and reduces at higher frequencies. Clearly a methodology is required to optimise the resonator system to have a good sensitivity and also low mechano thermal noise. A gyroscope could be designed with increase number of fingers to get the higher capacitance variation caused due to Coriolis force but this would increase the damping and hence increase the mechano-thermal noise. In the forthcoming chapters the optimization of the design will be discussed in detail.

Chapter 4

Dual Mass Gyroscope Design

4.1 Introduction

The issue with the single mass gyroscope is that there is cross-coupling [19] and the capacitance variation achieved could be due to cross-coupling and not necessarily due to secondary mode deflection. To remove the problem of cross-coupling and increase the mass (for higher sensitivity) several designs were studied.

4.2 Dynamics of Dual Mass Implementation

The structure of the two mass gyroscope is illustrated in 4.1 Here there are two sets of

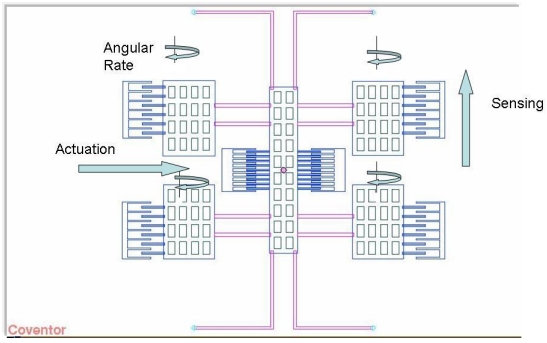

Figure 4.1: Dual Mass Implementation of Gyroscope in Coventorware

masses ;an interior and four masses suspended by straight beams. The inner mass is actuated electrostatically as discussed in the previous chapter. When the gyroscope is subjected to an angular rotation, a Coriolis force is induced in the direction orthogonal to the drive-mode oscillation at the driving frequency. The oscillation in the outer masses induced due to Coriolis force is sensed by the set of parallel fingers which act like a set of capacitors. 4.1. The symbolic representation could be done as in 4.2

The dynamic equations for the 2 mass gyroscope is given as

$$m_x\ddot{x} + c_x\dot{x} + k_x x = F\text{actuation} \qquad (4.1)$$

$$m_y\ddot{y} + c_y\dot{y} + k_y y = 2\mathrm{m}_y \times \Omega_z\dot{x} \qquad (4.2)$$

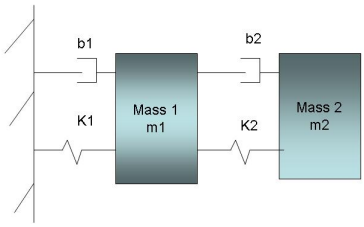

Figure 4.2: Lumped Parameter Model of 2-Mass Gyroscope

Here in eq(4.2) the Coriolis force component term has mass m_y which corresponds to the outer masses. The primary mass m1 is suspended by Lbeams and is tuned to resonate in x direction. As the outer masses are connected to the inner mass through straight beams ,they also resonate in x-direction. However, the Lbeams do not allow the inner mass to move in Y direction when an angular rate is imposed ,hence the inner mass is decoupled. Straight beams on the other hand are tuned to allow the movement of secondary masses in Y-direction when an angular rate is imposed. To keep the uniformity and to ease tuning of k/m ratios, four uniform masses are suspended.

4.3 Preliminary Designs and Simulations

We would discuss here the first two preliminary designs and the simulation results corresponding to them. In Figure 4.3 two dual mass designs are presented.

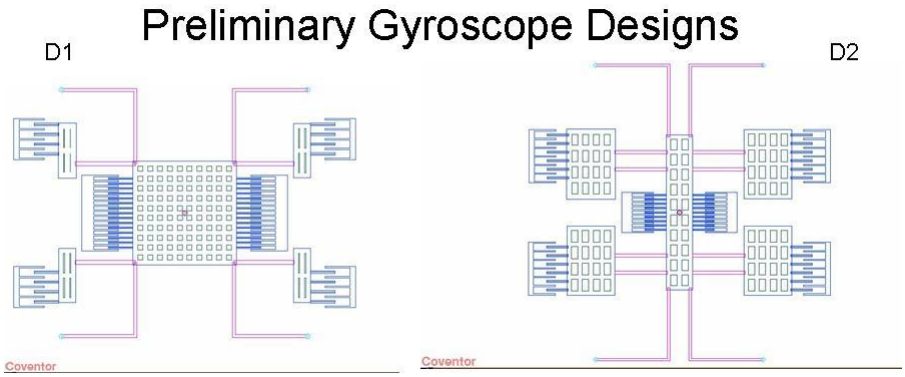

Figure 4.3: Schematic of Preliminary Dual Mass Gyroscopes D1 and D2

In design D1, we could see that the inner mass is bigger than the 4 outer masses.The inner movable structure has dimensions of $200\mu m$ by $200\mu m$ and outer of $100\mu m \times 25\mu m$. The lbeams which support the inner mass have the dimensions of L1 ,L2 as $150\mu m$ and widths of $6\mu m$. The straight beams have lengths of $122\mu m$ and width of $6\mu m$, here thickness of the silicon considered is $12\mu m$. In design 2,we have inner mass of $50\mu m \times 350\mu m$ with thickness of $12\mu m$. Each four outer masses are made up of $100\mu m \times 200\mu m$ with thickness of$12\mu m$. The holes in the outer masses are of $13\mu \times 38\mu$ with numbers 16 in each. The holes in the inner masses are of $15.0\mu m \times 24.0\mu m$ with 20 in total.

An AC analysis for both the designs is shows in Figure 4.4. Design D1 has the matched resonant frequencies at 58570Hz and design D2 had matched frequencies at 33516 Hz.

4.3.1 Consequence of the Analysis

Design D1 doesn't look robust as it has only one straight beam supporting each outer mass. The external masses are also too small. The mass of the primary mode could be reduced and the mass in the secondary mode increased. Hence the design D2 was implemented.

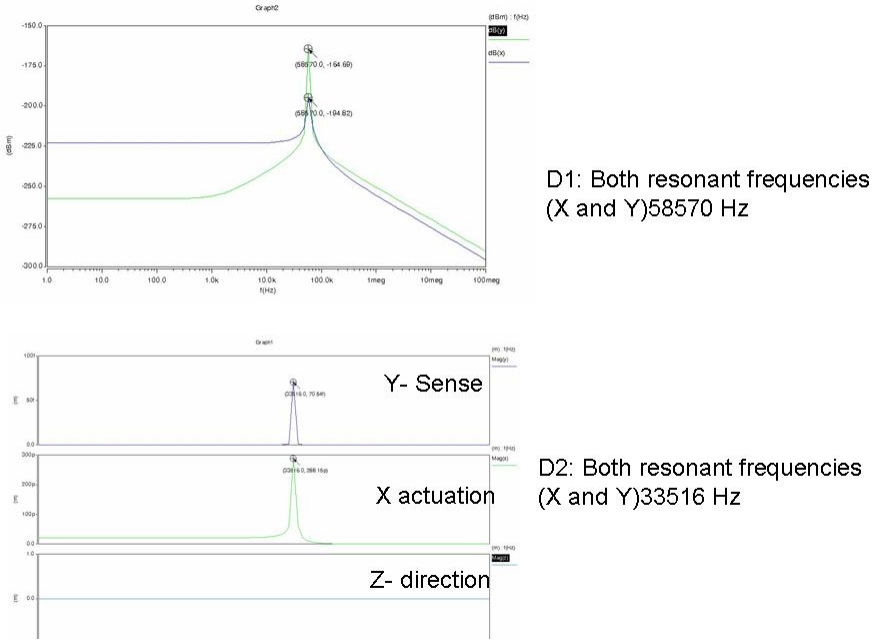

Figure 4.4: AC analysis D1- matched frequency ;58570Hz D2-matched frequency 33516Hz

4.3.2 Transient Analysis

Time domain analysis is illustrative for the behavior of the gyroscope when an angular rate is applied. Saber Sketch is used to simulate the gyroscope. In figure 4.5actuation is done by imposing a harmonic motion along X-axis and zero velocity in Y and Z direction. When an angular velocity of 1 rad/s is imposed there is some displacement in Y direction as seen in 4.6. The transient response of the design D2 and is shown in this analysis.

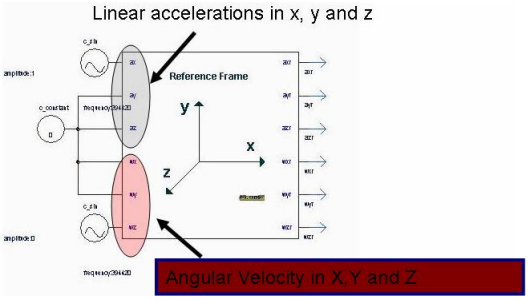

Figure 4.5: Symbolic representation in Saber Sketch for Characterization

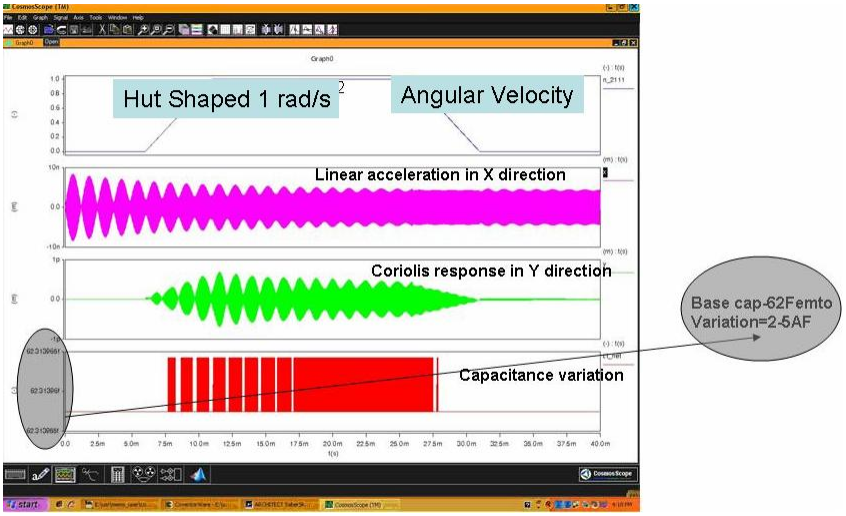

Figure 4.6: Transient Analysis-Impact of Coriolis Force,Displacement in Y and X Direction observed

Methodology

In this simulation set up transient analysis is performed to see variation of capacitances in the outer masses with the sensing direction.

Method: Transient analysis is performed for a total duration of 40ms. An angular velocity of 1 rad/s is applied at z direction. Note : To carry out the transient analysis, linear acceleration is applied in the x direction at 33516 Hz.

Simulation Result: we observe a non zero y displacement only when there is angular velocity in the z direction. Capacitance variation (sum of top left and top right capacitances) of comb drive also follows with the y.*Note* that the capacitance variation observed is taken only from one of the external masses. Net capacitance would be the sum of all four masses.

4.3.3 Capacitive Detection

In Figure 4.7 are of 2u in width and 50u in length pitch: 15u : 56 finger:40u threshold is 1.5u

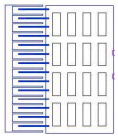

Figure 4.7: Capacitive Fingers and Capacitive Detection

C1= ϵ×overlap area×displacement/ (g0+lateral threshold) (4.3.1)

C2=$\epsilon\times$overlap area$\times$displacement/ (g0-lateral threshold) (4.3.2)

$\triangle$ C= $2\times\epsilon\times$overlap area$\times t\times$displacement/ $(g0)^2$ (4.3.3)

Cap sense= $2\times\ 8.8412\times10^{-12}\times40\times12\times10^{-12}\times2.02\times10^{-9}/(5.5\times10^{-6})^2$ (4.3.4)

Total number of fingers are 56 which results in capacitance variation of 32.7 aF for an input signal of 1 rad/s. Table 4.1 gives the approximations of the capacitance variation with different number of fingers and the distance between them.

Initial gap	5.5μ	4.5μ	4μ	3.5μ
Number of fingers	56	72	80	88
$\triangle C_0/rads^2$	31.37 aF	60.954 aF	87.07aF	123aF

Table 4.1: Capacitance Variation with Different Parameters

4.3.4 Consequence

The Design D2 behaves like a gyroscope and can be designed to have a better sensitivity than D1. The design was done assuming the thickness of the structure to be $12\mu m$, this could be increased to $20\mu m$ using the latest SOIMUMPS technology. The number of fingers could be increased to enlarge the sensitivity(provided the extra damping,introduced by a larger number of plates, is not significant).The next chapter of thesis describes the fabricated structures.

Chapter 5

Implementation of the MEMS Structure

5.1 SOIMUMPS Technology

The SOIMUMPS technology stands for Silicon-On-Insulator Multi User MEMS Processes [13].The SOI-MUMPS process has only three layers. 1) Silicon(structure) with thickness $10\mu m$ m or $25\mu m$ for the development of the micro-gyroscope ,25μ m thickness silicon was chosen;2) oxide layer on top of the substrate is about 1+/-0.05 μm m 3) the handle wafer (substrate) about $400\mu m$ thickness. Metal padding is done over the structure for the electrical connections and is gold plating of 0.52μm thickness. A typical cross-section looks like 5.1

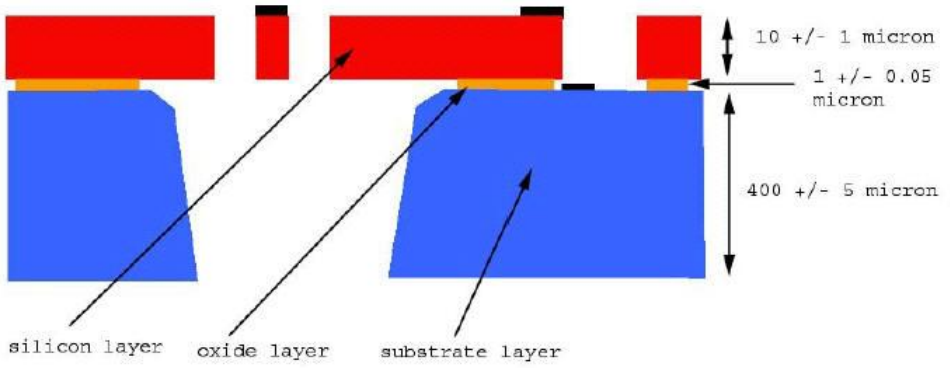

Figure 5.1: SOIMUMPS technology fabrication [13]

In figure 5.2 a gyroscope using the SOIMUMPS is fabricated outside. Region A is the silicon 400 , region B is the active silicon on which the structure is machined(25μm),C is the padmetal and D is the trench made from the back etching.

The design has to confirm with a set of design rules,provided by the SI-foundry(minimum feature size,minimum distances, etc). For the connections and the pad-metals the minimum feature size and spacing are 3μm ,for SOI 2μ m while for trench it is 200 μ m respectively. The issue with the gyroscope design was that the design is spread out and has many parts under trench ,so lot of care was required while placing the combdrives as the minimum

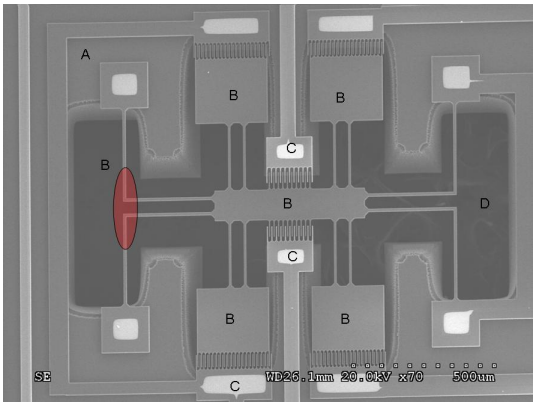

Figure 5.2: SOIMUMPS Gyroscope fabrication

feature of the trench is 200μ m and the spacing between the trenches is 200 μm . A risk was taken while making the layout of figure 5.3 as the undercutting of the trench could release certain anchored shapes.

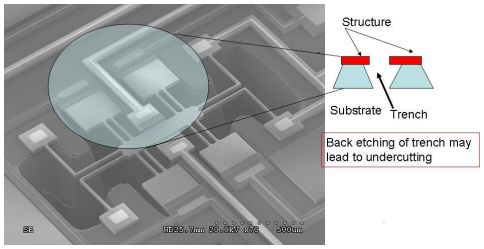

Figure 5.3: SOIMUMPS Gyroscope fabrication with Undercutting

An alternative design was formulated by taking the actuation outside to make structure more stable and two beams of 400 μm $\times$20μ m are suspended and the capacitive fingers are attached there as seen in 5.4

The micro machining of the fingers is very crucial and care has to be taken that the fingers don't get stuck to each other. Small bumps (2μm diameter)to avoid large area contacts,leading to stiction as seen in figure 5.5

The interconnections are crucial for actuation and sensing metal lines have to be laid on the silicon to get high conductivity but enough spacing should be left in accordance with the design rules.

5.2 Fabricated structures

Two final structures were finalized for the analysis D1Cross -o-scope and D2 Alternative gyroscope. A thorough analysis would be done on them and their results discussed. Both

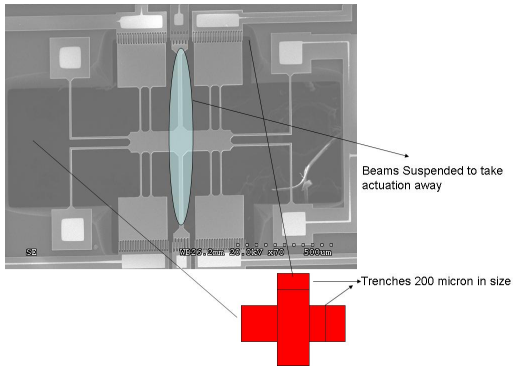

Figure 5.4: Gyroscope Design taking the actuation away

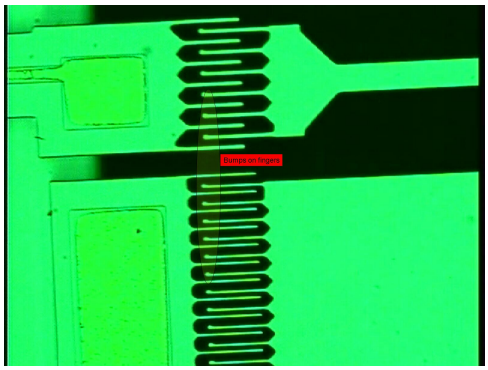

Figure 5.5: Bumps on fingers to avoid sticking

structures as seen in Figures 5.6 and 5.7 have the similar dimensions except for two masses of $400\mu m \times 20\mu m$in the case of the cross-o-scope

In the case of D2 design , the blue layer is the structure, red is the trench layer and green is the pad metal. In the case of the cross-o-scope red layer is the trench and green shows the silicon on which the structure is machined.

5.2.1 Suspension Design

Suspension beams have been analysed in the previous chapter. Here the computation is done for this specific case. The straight beams connect the primary mass with the four secondary masses. The secondary masses have to be tuned in such a way that they are free to move in the Y direction and stiff in the X direction (the actuation direction). In Figure 5.8 we see the straight beams supporting the mass. The length of the beams is 222μm ,width 8μm and thickness is 25μm.

Stiffness in the Y direction is given by $K_y = Etw^3/L^3$ and in our case it gets computed as 74.0331 N/m , the stiffness in X direction would be given as $K_x = Etw/L$ and would

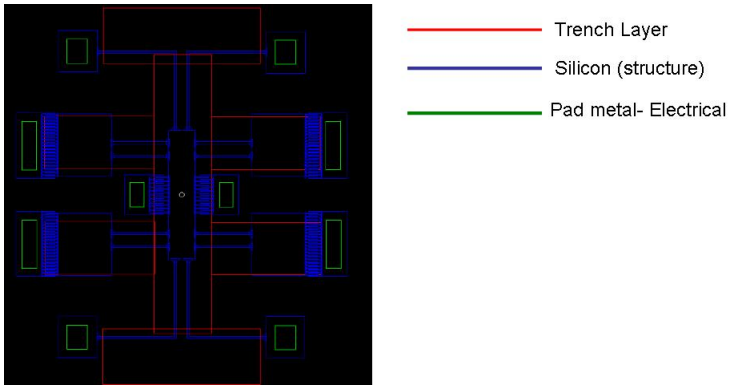

Figure 5.6: Alternate gyroscope

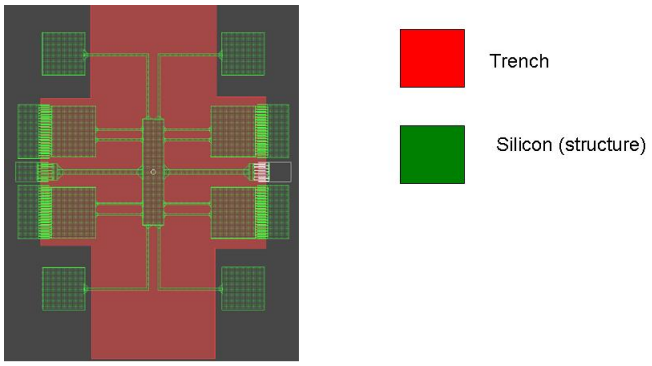

Figure 5.7: Cross-o-scope with actuation away

result in 27027.02 N/m (w^2/L^2) higher than in Y direction. This confirms that the beams would be easy to move in Y direction than in X direction. There are 8 beams which support the secondary masses, hence their net stiffness in the Y direction would be 592.10648N/m.

In the case of the Lbeam, (supporting the primary mass)has dimensions as 300μm in lengths, thickness is 25 μ m and the width as 10μm for each beams.

Here the stiffness in the Y and X directions would be computed in accordance with eq(5.1) and eq(5.2)

$$K_x = E.t.w_x^3.(l_x + 4.l_y)/{l_x}^3.(l_x + l_y) \quad (5.1)$$

$$K_y = E.t.w_y^3.(l_y + 4.l_x)/{l_y}^3.(l_y + l_x) \quad (5.2)$$

This gives K=347.52 N/m for each l-beam.As we have four of them the net stiffness is computed as 1388.5N/m in both X and Y direction.

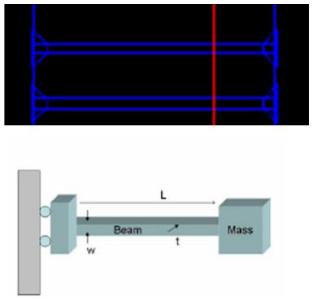

Figure 5.8: Straight beam

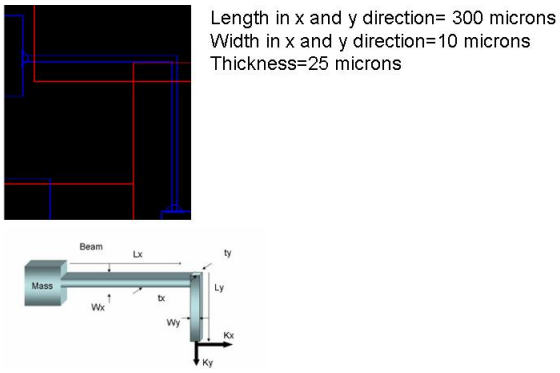

Figure 5.9: L beam

5.2.2 Damping Estimation

Damping analysis is essential in the dynamic modeling of the gyroscopes as their sensitivity is generally limited by the mechano-thermal noise generated by the interaction of the movable structure with the surrounding fluid, of a certain viscosity(damping). In our case the actuation is done in the X-direction and sensing in the Y direction. The actuation would lead to slide film damping and the sensing would lead to squeeze film damping. A 3-D model of the structure is shown on which meshing was done for the damping analysis as seen in figure 5.10.

The Slide film damping usually doesn't have any stiffness force and has only damping force variation with respect to frequency. The distance between fingers is $10\mu m$. Damping analysis results are shown in Figure 5.11 Interestingly the slide-film damping is not prominent for frequencies lower than 10^9Hz while the gyroscope usually operates at about 20-30kHz. This suggests that slide-film damping has a negligible contribution for the normal operation modes.

The squeeze film damping is carried out by displacing secondary masses in the y direction. Fingers in the secondary masses are designed such that one finger is separated by 6μm and other is separated by 8.5μm. The result of squeeze film damping analysis are shown in

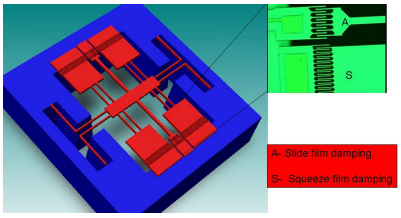

Figure 5.10: 3d Model on Which Dmping Analysis was Done

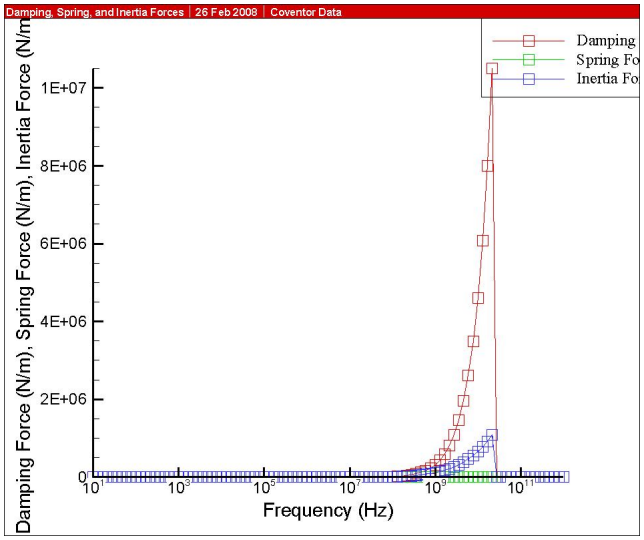

Figure 5.11: Slide Film Damping Analysis

Figure 5.12

Here the damping force is at the highest at about 10^5 Hz and then drops in magnitude. Most notedly the stiffness force increases with the frequency. The damping in Figure 5.12 gives the frequency dependency of the equivalent gas damping and spring constants, b(jω) and $k_d(j\omega)$.It is also visible that the elastic behavior($K_d(j\omega)$) of the air-structure interaction starts dominating over the damping component(b(jω)) at high frequencies.

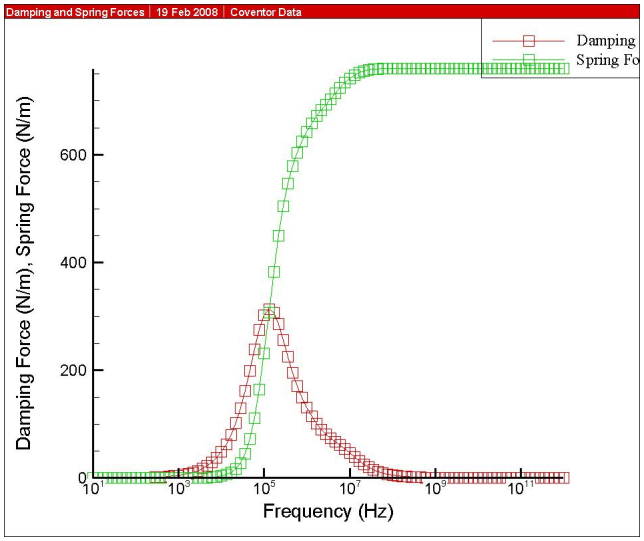

Figure 5.12: Squeeze Film Damping Analysis

5.3 Simulation Results

5.3.1 Frequency Response/Quality Factor

Frequency response of both analysis structures show similar results. We will look at the Quality factor and the AC analysis results. In the Figure 5.13 the resonant peaks happen for both the actuation mode and the sensing mode at 23101 Hz.

Here the Quality factor would be computed as the $Q = \Delta Y_{fo}/\Delta Y_{dc}$ and by computing we get the quality factor of 31.6227 . In our case we had to take the square root of the computation as the response got is after imposing the Coriolis force. The bandwidth of the structure is 730.51Hz($BW = f_0/Q$)

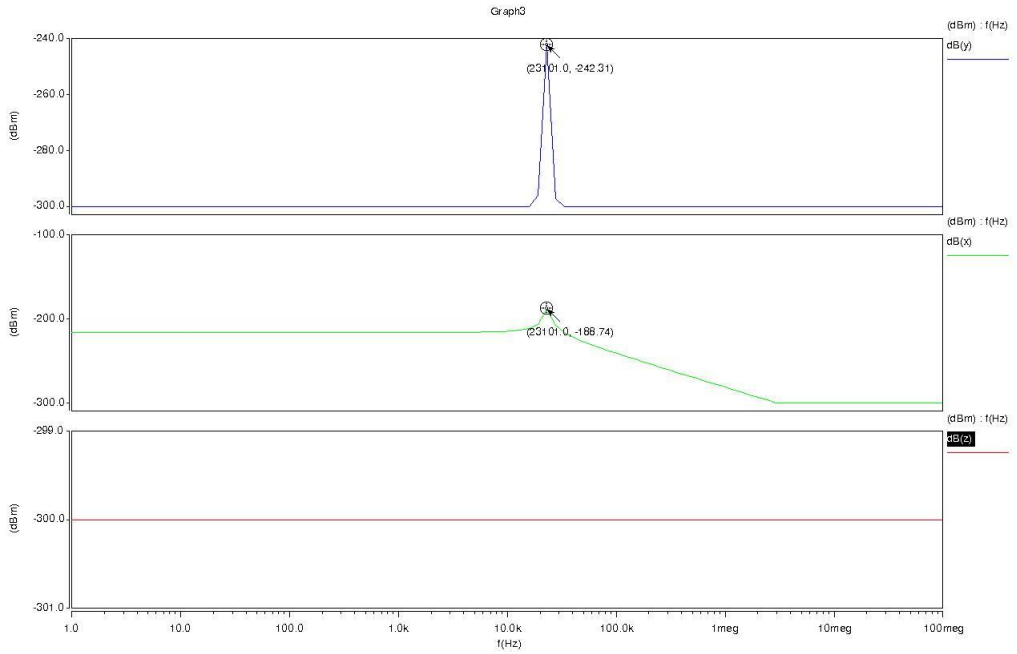

Figure 5.13: Ac Analysis, Blue Curve is the Sense Direction Response,Green is the Drive Mode Response,Bottom most Curve Shows the z Direction Response

5.3.2 Transient Analysis

In this simulation set up transient analysis is performed to see variation of capacitances in the outer masses with the sensing direction.
Goal: Sensitivity

Method: Here transient analysis is performed for the 40ms duration. An angular velocity of 1 rad/s is applied at z direction. Note : To carry out the transient analysis, linear acceleration is applied in the x direction at 23101 Hz.

Simulation Result: we observe that the signal y arises only when there is angular velocity in the z direction. The capacitance (sum of top left and top right) capacitances of comb drive also follows with the y in figure 5.15.

This proves that there is Coriolis Effect acting on the outer masses.

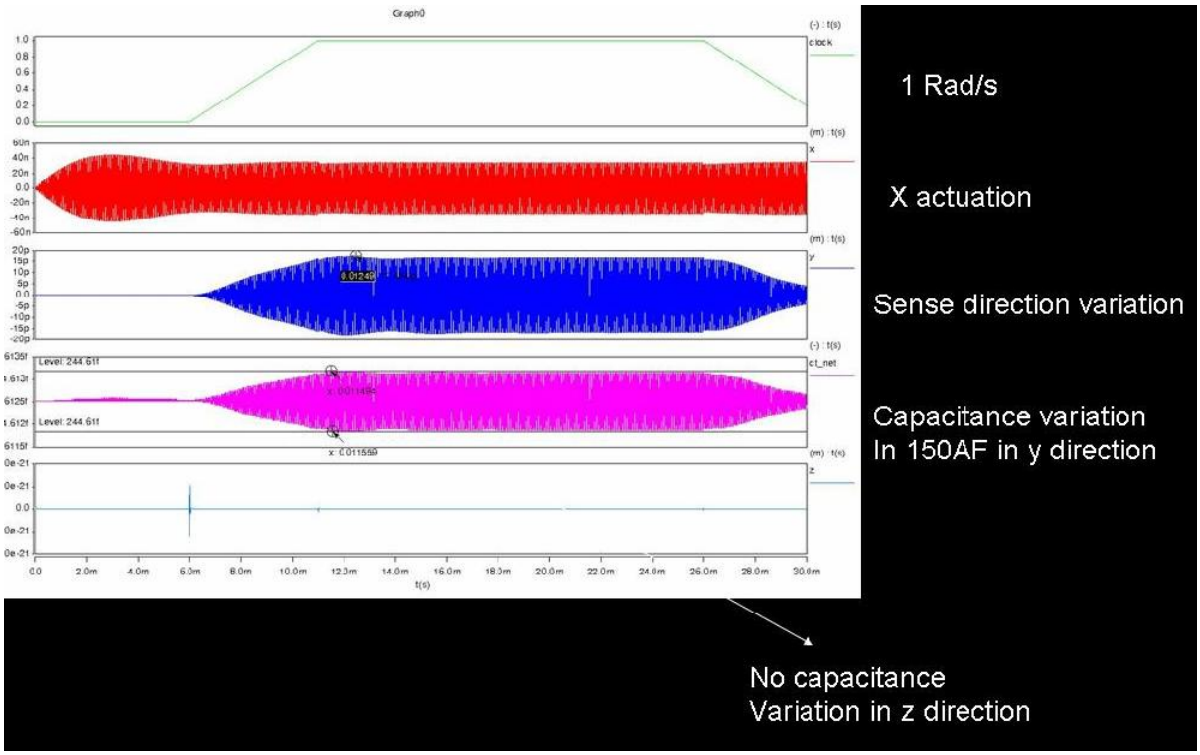

Figure 5.14: Transient Analysis- Alternate Design

A similar analysis carried out for the cross-o-scope showed a capacitive variation only in the negative direction. This could be due to the extra beams hanging. There is also some capacitance variation in the Z direction ,the reason could be the same.

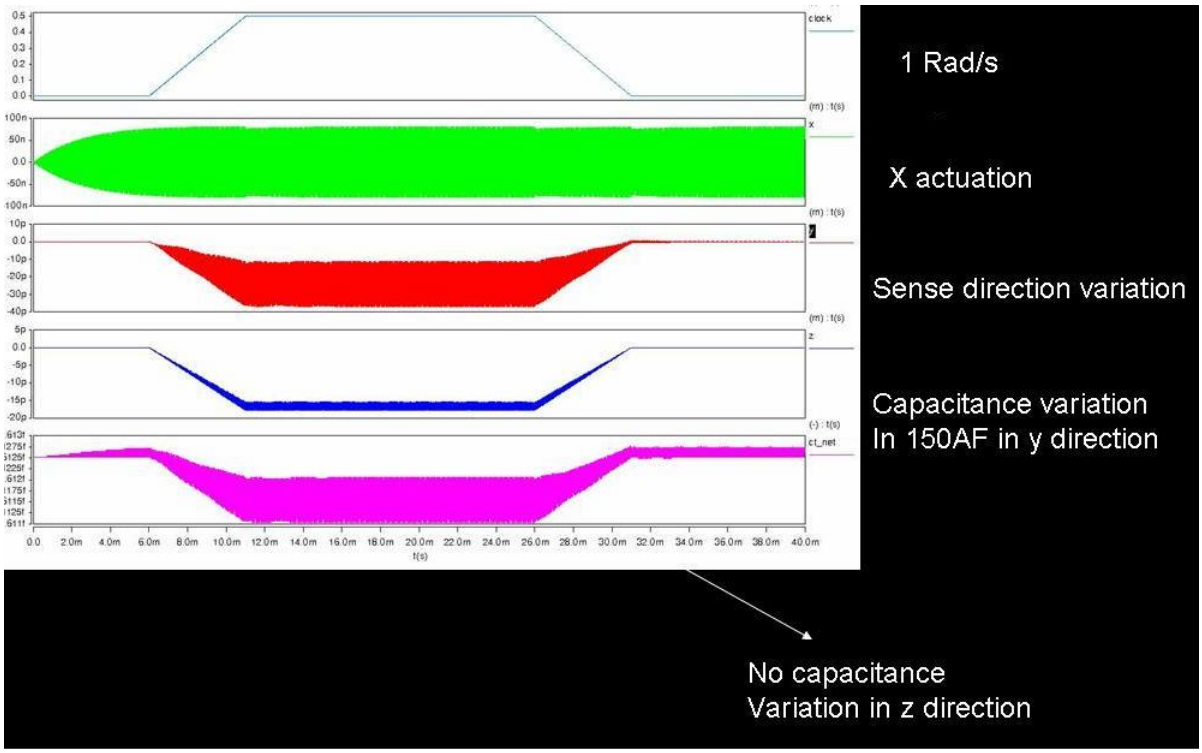

Figure 5.15: Transient Analysis- Cross-o-scope Design

5.3.3 Capacitance Detection

Method: Vac is applied from 5-25volts(keeping Vdc at 10volts) and is observed that displacement of 2.02nm is obtained in y direction when 25volts amplitude of ac is applied as shown in the 5.16 The capacitance variation at the displacement of 2.02nm is given as follows

$C_{sense+} = \epsilon \times t \times l \times N/(y + y_0)$ (5.3.2.1)

$C_{sense-} = \epsilon \times t \times l \times N/(y - y_0)$ (5.3.2.2)

Hence the net capacitance is given as

$\triangle C = C_{sense+} - C_{sense-}$ (5.3.2.3)

$\triangle C = 2 \times \epsilon \times t \times l \times N/y^2$ (5.3.2.4)

In the equation (5.3.2.4), y_0 is 4.25 μm,ϵ as 8.8412$\times 10^{-12}$ F/m,area over lap as 800 $\times$ $10^{-12} m^2$ and the capacitance variation for 80 fingers is computed as 126aF.

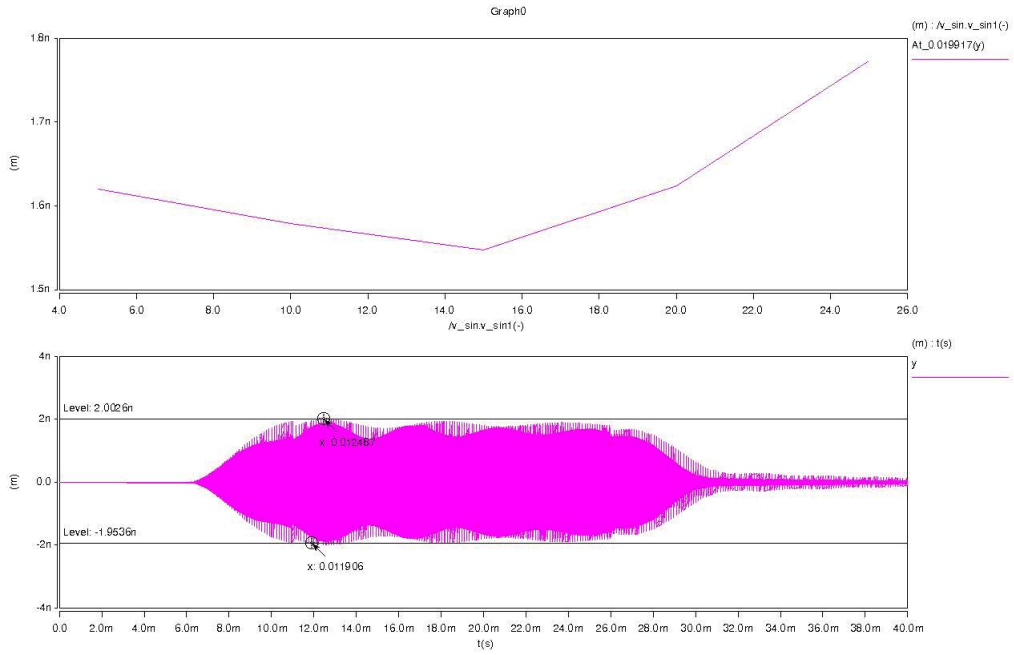

Figure 5.16: Displacement of 2.02nm in y Direction when Displacement of 3μm in x Direction is Imposed. (Top Graph Shows that to get 2.02nm Displacement ,25 v Ac is Required)

Chapter 6

Experimental Results

Pull in tests can identify if the devices actually move. The value of pull-in and release voltages can be used to identify the stiffness constants[16]. The setup requires DC voltage sources a probe station and controlled software to get the Current Vs Voltage and resistance Vs the voltage graphs. The probes are connected to bond pads as in Figure 6.1. The DC

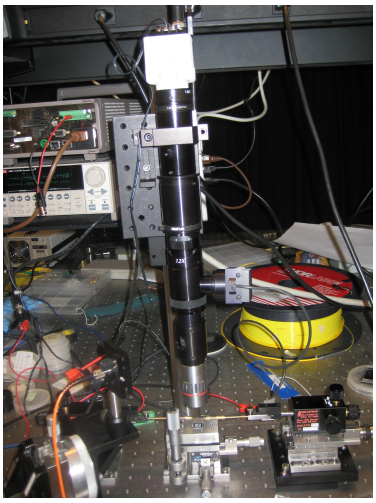

Figure 6.1: Probes connected to the devices to perform pull in test

voltage source was added to the secondary masses as seen in figure 6.2.

6.1 Methodology

The voltages where slowly applied between the plates of the sensing capacitor and the reference limiting the current to 15μA and varying the DC voltages from 40-65 Volts. Figure 6.3 shows the variation of the current Vs voltage, at about 54.5 V, the current shoots up and there is a clear short circuit between the fingers of the secondary masses(electrostatic forces>mechanical forces). When the voltage was reduced from 65 to 40 volts we see that there is release of snapped fingers at 48.3V and this is called the release voltage.

These tests were performed repetitively to get the final value as seen in figure 6.4

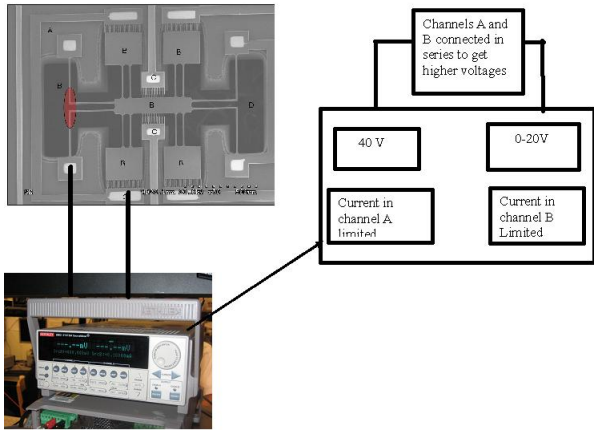

Figure 6.2: Probe Attached to the Secondary Mass and Other to the Ground Bondpad/Connections of Keithley box(DC source)

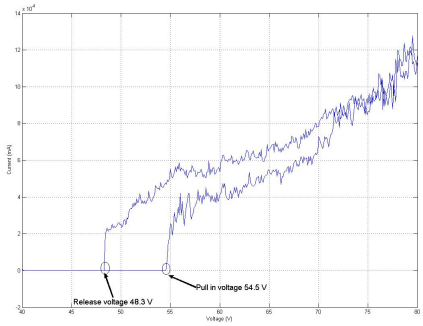

Figure 6.3: Release and Pull in Voltage of the Alternate Design

The cross-o-scope was also set up for the dc test as discussed above and showed that the resistance is very high at about 22.5 Kilo ohms and about 63 Volts we see in figure 6.5that the resistance drops to zero and the capacitive fingers are touching each other producing a short circuit.

These tests were also carried out repetitively to see the robustness of the devices. The results are illustrated in figure 6.7

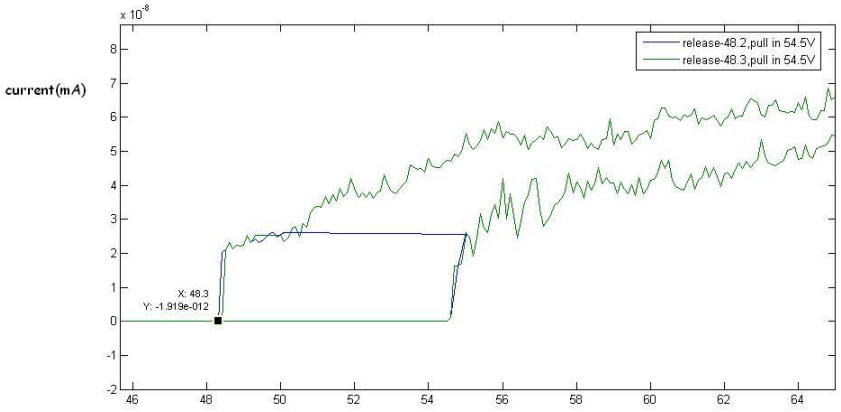

Figure 6.4: Release and Pull In Voltage of the Alternate Design on two Different Designs

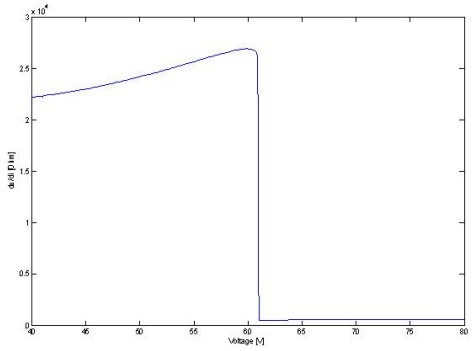

Figure 6.5: Variation of the Resistance Vs Voltage

6.1.1 Verification of the Pull In Results

The experimental results could be used to quantify the stiffness coefficient of the beams which suspend the secondary masses. To quantify the results ,analytical modeling is checked with sabe simulations. According to the theory the pull in happens when the electrostatic forces get higher than the mechanical force (when stiffness of the beams are not strong enough). The pull-in phenomenon is described in Figure 6.8

Pull in voltage is given by [16]

$$V_{pi} = \sqrt{\frac{8kd_0{}^3}{27C_0}} \qquad (6.1)$$

Here k is the stiffness,d_0 is the distance between the two plates,C_0 is the initial capacitance. This equation could be rewritten in the form of K as it is the unknown.

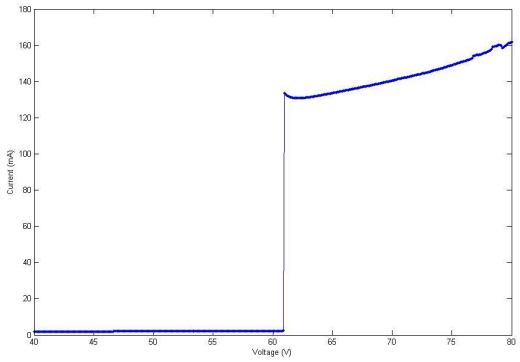

Figure 6.6: Variation of the Current Vs Voltage Pull in at 63V

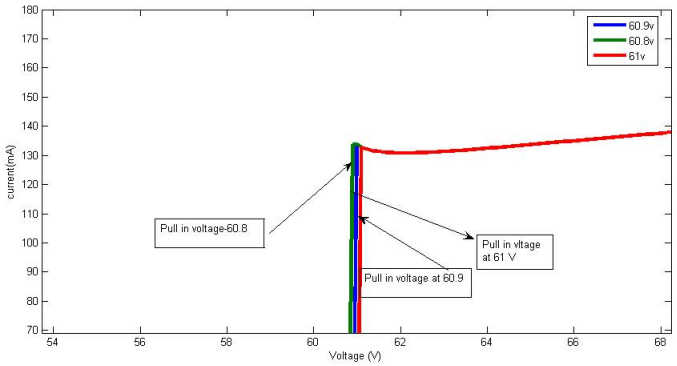

Figure 6.7: Variation of the Current Vs Voltage pull in for Different Devices

$$K = (27/8) \times C_0 \times {V_{pi}}^2 \qquad (6.2)$$

The values obtained from the experimental measurements are plugged in the equation and the stiffness coefficient is obtained,further the analysis is also checked using the macromodel of saber sketch.

Stiffness of two beams which support the mass is given by the $2 \times Etw^3/L^3$,where $t = 25\mu$, $w = 6\mu$, $L = 222\mu$ and E as 150GPa .The stiffness is evaluated as 148.0663N/m and for E=163GPa ,the net value is 160.8987N/m. To check with the macromodel of Saber ,the setup as shown in Figure 6.9

When a transient test was done on the beam to see how its deflection varied with the force as seen in figure 6.10

In Figure 6.10, stiffness is computed by dividing force by deflection and is seen as the ratio of 5.458×10^{-6}N to 65.433×10^{-9}m which is 83.4 N/m. As there are two beams which

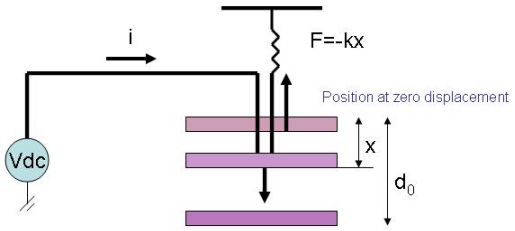

Figure 6.8: Electrostatic and Mechanical Force Balance

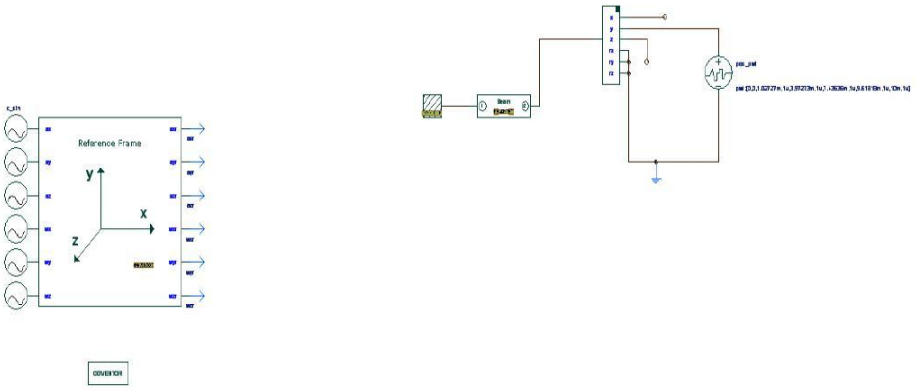

Figure 6.9: Force is Applied at the End of the Straight Beam with Same Parameters

suspend the secondary mass the net stiffness would be 166.8 N/m, which is near to both the experimental and analytical values

- Stiffness (Experimental):63V-168.8694 N/m
- Stiffness (Analytical):Using Formula - 148.0663N/m(E=150GPa),160.8987 N/m(E=163 Gpa)
- Stiffness-(Macromodel):Saber-166.800 N/m

For the alternate gyroscope(D2 Design) the pull in voltage experimentally obtained is 54.5V and gives the following results.

- Stiffness (Experimental):54.5V-124.3932 N/m
- Stiffness (Analytical):Using Formula - 148.0663N/m(E=150GPa),160.8987 N/m(E=163 Gpa)

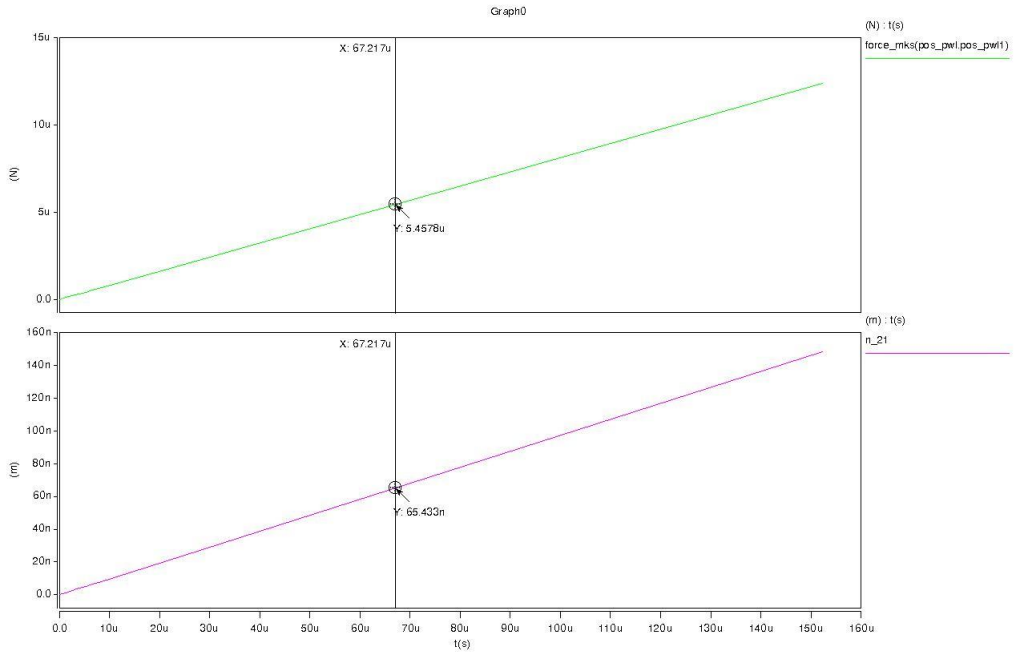

Figure 6.10: Linear Variation of Force And Displacement

- Stiffness-(Macromodel):Saber-166.800 N/m

The alternate gyro(D2 Design) experimentally shows that the stiffness constant is lesser than what is computed.

6.2 Experimental Set Up for The Characterization of Device

Although the movable structure oscillates mainly in the plane, there is also vibration in the vertical direction, and the y-axis resonance frequency is simulated to be 23kHz, as is shown previously in figure (5.12) of previous chapter.

This vibration can be detected using a Laser Doppler Velocometer (LDV), which is introduced in [23].The oscillator characterization setup is shown in Figure 6.11 DC bias and AC signal are applied on the gyroscope through probes and contact pads, and both continuous and pulsed signals can be used to actuate the device.

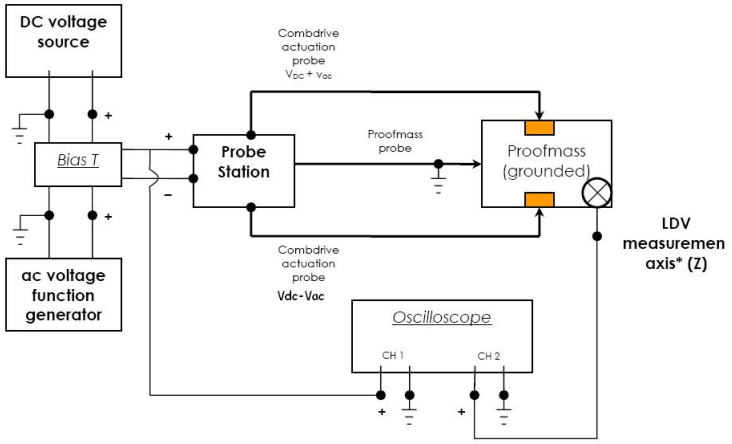

Figure 6.11: Schematic View of Gyroscope Characterization Setup. The z-axis Vibration is Measured by LDV.

The z-axis vibrations are measured by the LDV on top, which takes advantages of optical interferometry and Doppler Effect. Both the actuation signal and the vibration signal are monitored by an oscilloscope. The actual characterization setup is shown in figure 6.12.

The current design of the gyroscope has less number of fingers and requires large voltages to put proof mass in resonance. A better design has to be made with increase in number of capacitive fingers. The gyroscope is designed to resonate and sense in-plane motions. The LDV could be used only for out of plane motion but still could give some help as non linearities of the fabrication processes could lead to vibration of device in vertical direction. The test is still being carried out.

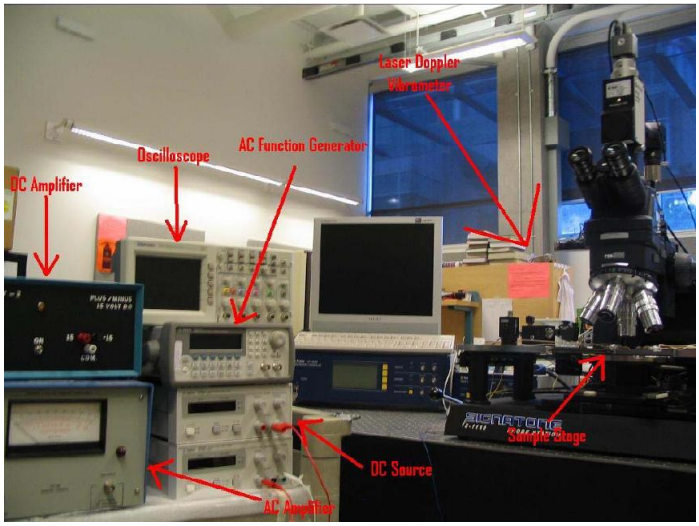

Figure 6.12: AC Analysis Stage

Chapter 7

Noise Analysis for Gyroscope Structure and Noise Based Optimisation

7.1 Introduction

A vibratory gyroscope device includes the micro-mechanical resonating structure, together with the associated electronics for actuation and sensing. 7.2 shows a generic system, together with the various noise components.

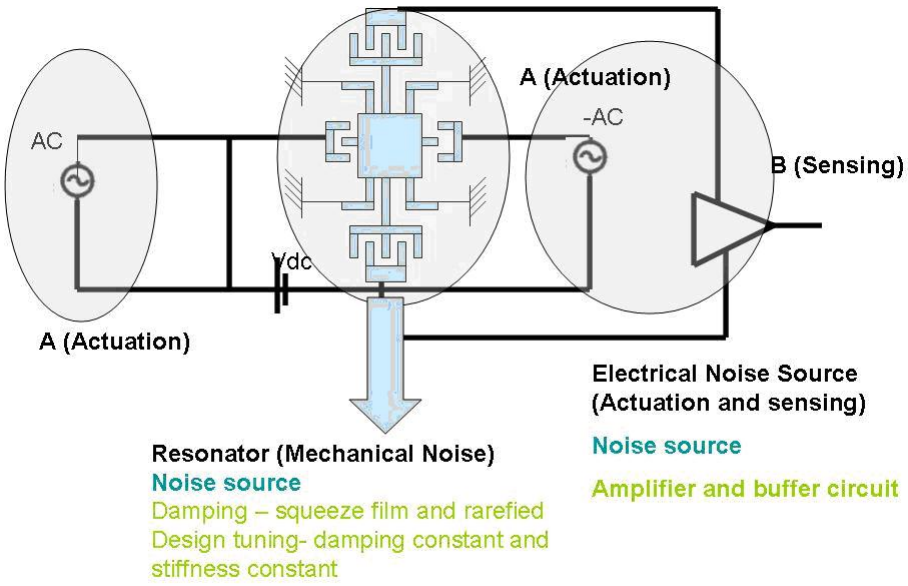

Figure 7.1: Gyroscope with Noise Sources

In the absence of an applied (electrostatic) actuation, the presence of losses into the system will continuously decrease the amplitude of mechanical oscillations. A simplified model of a resonant vibratory gyroscope including equivalent noise force terms is given by the following equations:

$$m\ddot{x} + c_x\dot{x} + k_x x = 2m \times \Omega_z \dot{y} + F_{noise}(c_x, t) \quad (7.1)$$

$$m\ddot{y} + c_y\dot{y} + k_y y = \text{-}2\text{m}\times\Omega_z\dot{x} + F_{noise}(c_y, t) \quad (7.2)$$

The noise forces in the above equations are correlated with the respective damping coefficients, in order to establish a thermodynamic equilibrium between the microstructure and the surrounding fluid. In thermodynamic equilibrium, as stated by the fluctuation-dissipation theorem, the energy lost by the system through damping is statistically balanced by the energy brought into the system by the equivalent noise forces $F_{noise,x}$ and $F_{noise,y}$. An overall noise analysis of the resonant structure makes use of the equipartition and Nyquist theorems. According to equipartition theorem, each energy storage mode in thermal equilibrium will have an average energy of $1/2k_BT$, where k_B is Boltzmann's constant and T is the absolute temperature. Nyquist's relation gives the spectral density of the fluctuating noise force F(f) related to any mechanical damping coefficient b(f) as:

$$\text{F}^2_{noise} = 4K_BTb(f) \quad (7.3)$$

The formula is valid even if the damping coefficient is frequency-dependent, but the usual mechano-thermal noise analysis in MEMS use a frequency-independent b value, as shown in figure 7.2,which illustrates the net noise in the system as the combination of the electrical and mechano thermal noise terms. For the mechanical subsystem, the practice so far is to estimate a constant value for the damping coefficient b in the operating frequency region of interest. In the case of resonant systems operating at or close to their resonance frequency f_0, the value of $b(f_0)$ is used for noise analysis, estimated from finite element simulations or experimentally measured. For systems operating in the low-frequency range, again a constant value of the damping is taken into account, usually estimated or measured at a central frequency in the bandwidth. In both operating regimes the approximation of a constant damping coefficient used for noise analysis might give erroneous results, especially if the functionality of the microsystem is inherently located over frequency regions where b(f) has a strong variation. A complex elasto-damping behavior of the fluid-structure interaction translates, due to thermodynamic equilibrium, into a similar frequency-shaping of the equivalent noise force. It is therefore necessary to include such frequency dependency into the noise analysis, in order to obtain a proper SNR estimation and optimization. Nevertheless, even state-of-the-art microsystem design tools (e.g. Coventorware) do not use macro models for frequency-dependent noise coefficients.

7.2 Semi Automated Tool for Noise Analysis and Optimization

The design and optimization flow procedure is illustrated in figure 7.3[14]. It is presently implemented as a combination of several design tools: structure design and finite element

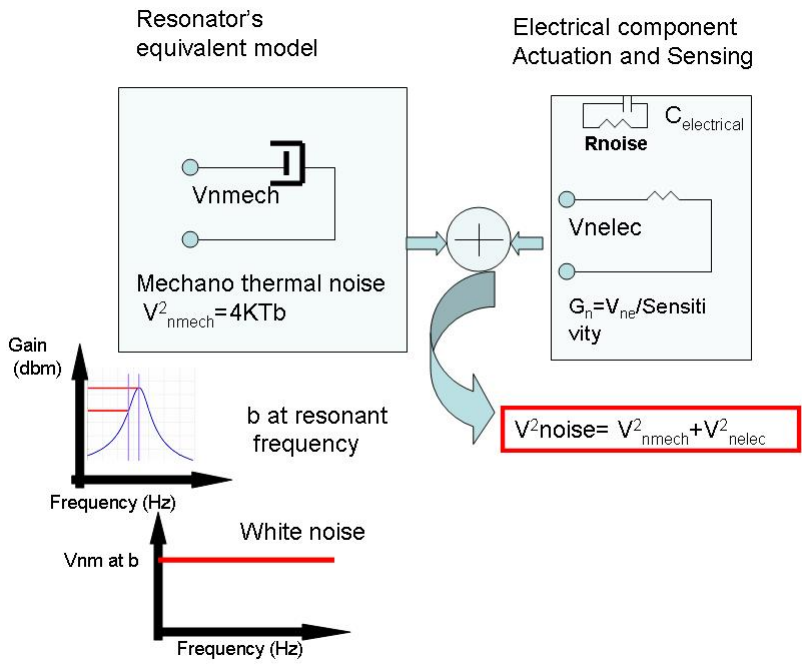

Figure 7.2: Gyroscope with Noise Sources

analysis of the damping are performed using Coventoware, while macromodel extraction and the combined numeric/symbolic optimization are presently done using Mathematica. Layout geometry is designed based on the given design rule set, followed by extensive finite element simulations (using MemMech module within Coventorware) of air-structure interaction for small vertical displacements of the mass. The result of the (time-consuming) finite element analysis step gives the frequency-dependency of the equivalent gas damping and spring constants, b(jω) and kd($j\omega$), as shown in Figures 5.11 and 5.12.

The results are then exported to Matlab as a list of values for b(jω), kd($j\omega$), corresponding to the simulated frequency points. Matlab is then used to create smooth interpolating functions for both b($j\omega$) and kd($j\omega$),which are used in the subsequent steps. From a noise analysis viewpoint, air-structure interaction has two direct consequences, as illustrated in 7.4: 1. A frequency-dependent noise force term is associated with the loss mechanism due to b($j\omega$) 2. A frequency-dependent elastic interaction, represented as an equivalent inductance L($j\omega$)=1/kd(jω), which will shape the transmission of the input noise to the equivalent output displacement noise.

7.3 Acceleration Noise/Output Displacement Noise

To estimate the influence of b($j\omega$) and k_d(jω) on the overall performance, both an equivalent input acceleration noise and an equivalent output displacement noise are computed

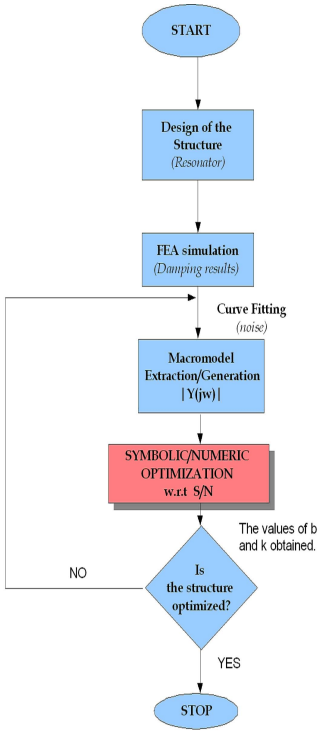

Figure 7.3: Noise Analysis and Design Optimization Flow Diagram

and compared with the common white-noise assumption. The equivalent input spectral acceleration noise is given by[14] as

$$Acceleration_{noise} = \sqrt{4K_B T b(j\omega)}/m \quad (7.3.1)$$

Figure 7.5 illustrates the variation with frequency of the equivalent input acceleration noise, compared with the frequency-independent model; in the last case, the low-frequency value of the damping coefficient (as extracted from finite element simulations) was extended over the entire frequency range (blue line curve).

The equivalent input noise limits the sensitivity of the device to external input inertial effects. It is therefore obvious from the previous figure 7.5 that the white-noise model will overestimate the noise, and does not lead to a potential noise optimization of the resonant structure. Considering the frequency-dependent behavior of the damping coefficient leads to the identification of reduced flat noise frequency-ranges, better suited for sensing external inertial effects.

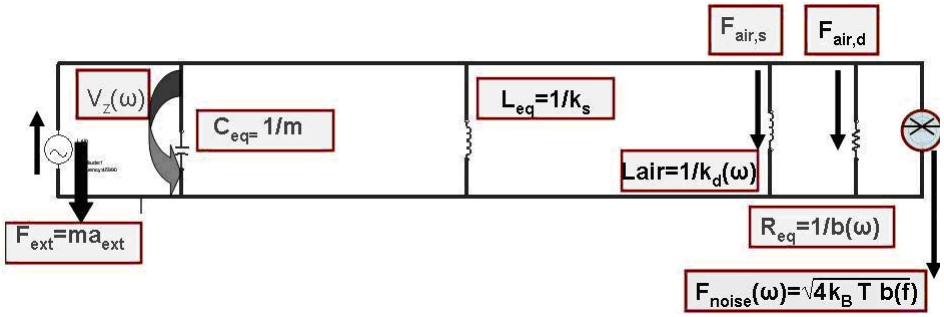

Figure 7.4: Macromodel For Noise Analysis

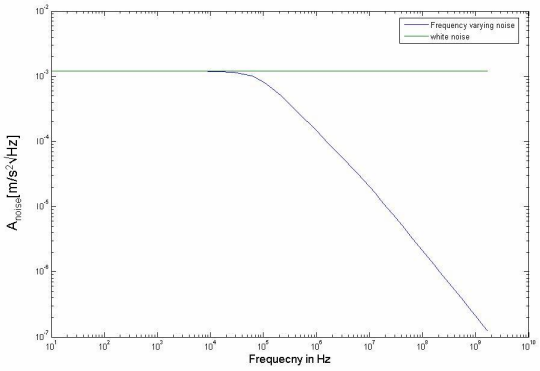

noise.jpg

Figure 7.5: Equivalent Input Acceleration Noise, Green White Noise Model/Blue Novel Methodology

7.3.1 Output Displacement Noise

To understand the noise analysis we take the block diagram of the gyroscope ,(see figure 7.6)

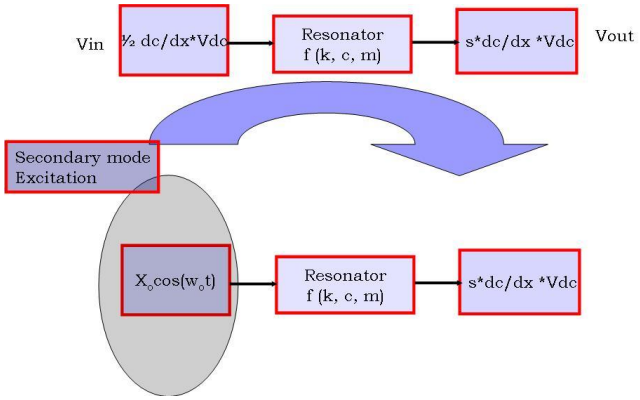

Figure 7.6: Transfer Function with Secondary Mode Excitation

To make things easier to compute we directly assume the secondary mode of excitation to be $X_o cos(w_o t)$. The dynamic equations of the gyroscope would be modified as

$$[m\ddot{y} + c_y\dot{y} + k_y y] = 2\mathrm{m}\Omega_z\dot{x} \quad (7.3.2)$$

Laplace transformation leads to eq(7.3.3)

$$[ms^2 + c_y s + k_y]Y[s] = 2m\Omega_z sX[s] \quad (7.3.3)$$

Laplace $\{X_0 cos\omega_0 t\} \equiv X_0(s/s^2 + \omega_0^2)$.

$$[ms^2 + c_y s + k_y]Y[s] = 2\mathrm{m}\Omega_z s^2/(s^2 + \omega_0^2) \quad (7.3.4)$$

Now by rearranging the terms we get

$$Y[s]/\Omega_z = 2\mathrm{m}\ \mathrm{s}^2/(s^2 + w_o s^2)(ms^2 + c_y s + k_y) \quad (7.3.5)$$

Term y/Ω_z gives the sensitivity (ie the deflection in the y direction per angular acceleration)

The damping coefficient C_y has two component 1)stiffness and 2) damping forces and could be modeled as $C_y = K_d + j\omega b(j\omega)$ the K_d term is obtained from FEA for a discrete frequency values and so is the frequency varying damping coefficient. Replacing the damping coefficient in eq(7.3.5)

$$Y[s] = (2m\Omega_z s^2 X_0)/(s^2 + \omega_0^2)\{ms^2 + (k_d + b(j\omega))s + k_y\} \quad (7.3.6)$$

This could be further simplified and is seen in eq (7.3.7)

$$Y[s] = (2m\Omega_z s^2 X_0)/(s^2 + \omega_0^2)\{(m+b)s^2 + k_d s + k_y\} \quad (7.3.7)$$

Simillarly displacement noise can be modeled as in eq(7.3.8)

$$\mathrm{Y}_{noise}[s] = (2\mathrm{ms}^2\Omega_z + \sqrt{4K_B T b(j\omega)})/(s^2 + w_o s^2)\{(m+b)s^2 + k_d s + k_y\} \quad (7.3.8)$$

The displacement noise could be analyzed by choosing the damping and stiffness values for a given resonant frequency as seen in figure 7.7

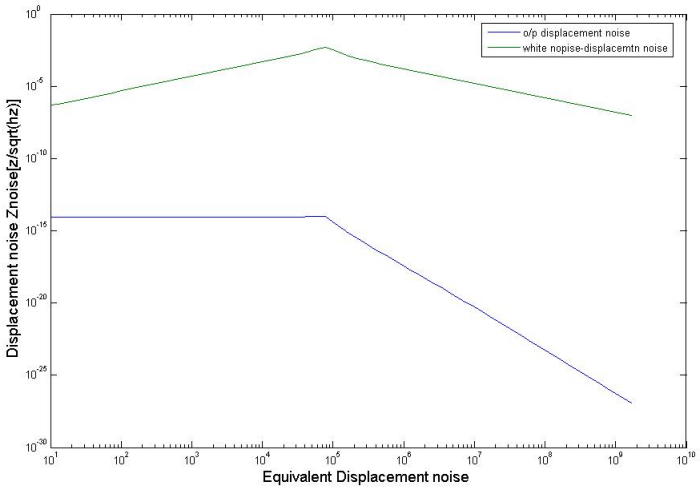

noise.jpg

Figure 7.7: Displacement Noise

Now the noise analysis has been defined and methodology defined, the net displacement Y would be given as[15]

$$Y_{output} = Sensitivity\Omega_z + Y_{noise} \quad (7.3.9)$$

Here sensitivity should be the highest and the displacement noise should be as low as possible to obtain an optimized structure.

Figure 7.8 shows equivalent output displacement noise and corresponding white noise approximations. Three different resonant frequencies are considered and the damping and stiffness coefficients are plugged into the transfer function as explained earlier in the section to observe the S/N variation with frequency.

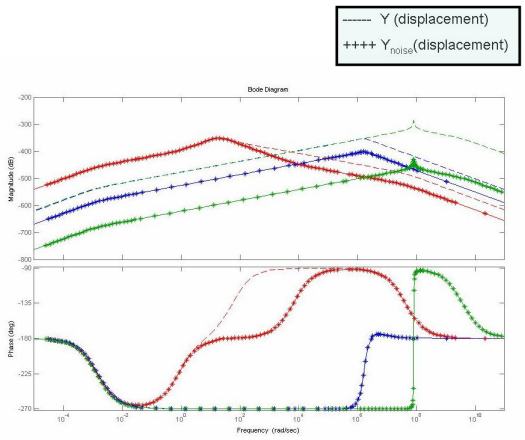

Figure 7.8: S/N Variation at Different Resonant Frequencies

The +lines indicate the S/N and − line indicates the white noise S/N approximation. Taking this example further, the experiment is repeated for more values of frequencies and is seen in figure 7.9.

In figure 7.9 the top graph the noise for 50Hz bandwidth is plotted for different frequencies. In the bottom graph of the 7.9,the$Y_{noise}$and sensitivity's magnitude is plotted as seen with the blue line ($Y_{output}withoutnoise$) and green line($Y_{output}withnoise$) .

The output of the system is given by eq(7.3.9)and magnitude of the Y_{output} decreases with addition of the noise component as can be seen that blue line is placed over the green line($Y_{output}withnoise$). It can be observed that the noise is at reduced magnitude for higher frequency ranges and it is tempting to design gyroscope at higher frequency but as also could be observed that the sensitivity reduces with the increase in the frequency range. An optimization is required to operate the gyroscope at frequency where the noise is limited and the sensitivity is good enough. In Figure 7.9 it can be seen that at about 10^6Hz there is an optimization.

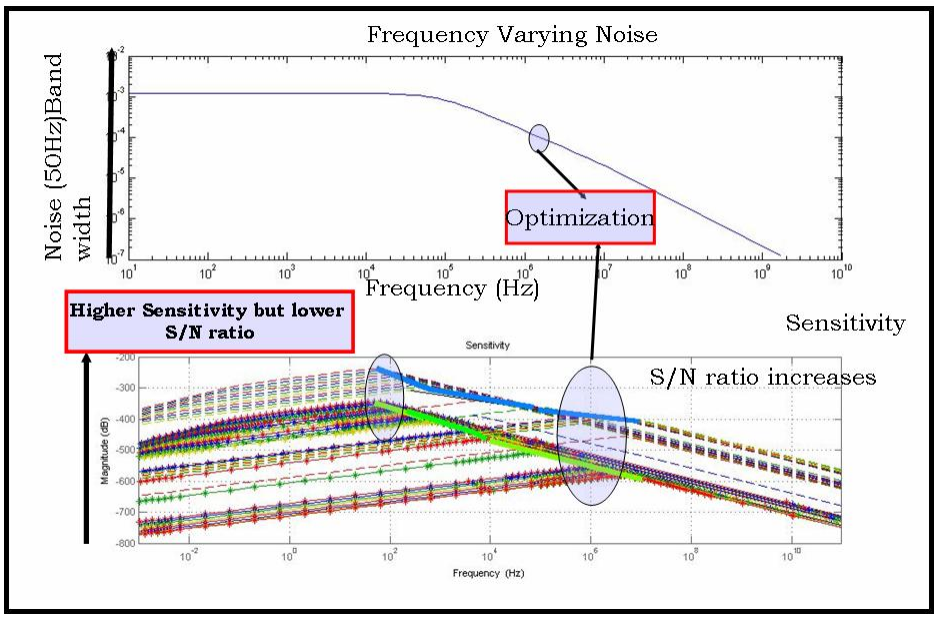

Figure 7.9: S/N Variation at Different Resonant Frequency/Acceleration Noise

Chapter 8

Conclusion and Future Work

A methodology for the design and analysis of MEMS-based gyroscopes was formulated and applied to the design and fabrication of a dual mass gyroscope.The parameters are given in 8.1. The fabricated gyroscopes are not an optimal design for the given technology.

X-Frequency	23101Hz
Y-frequency	23101Hz
Quality Factor	31.6227
Bandwidth	730.51Hz
Base Capacitance	244.6FF
$\triangle C/rad/s$	126AF

Table 8.1: Specification of Gyroscope

Nevertheless,the design can be adjusted to give either a high sensitivity by increasing the number of masses and tuning them to a particular frequency or to maximize the useful bandwidth by off-tuning them to a different frequency as seen in figure 8.1 The other benefit

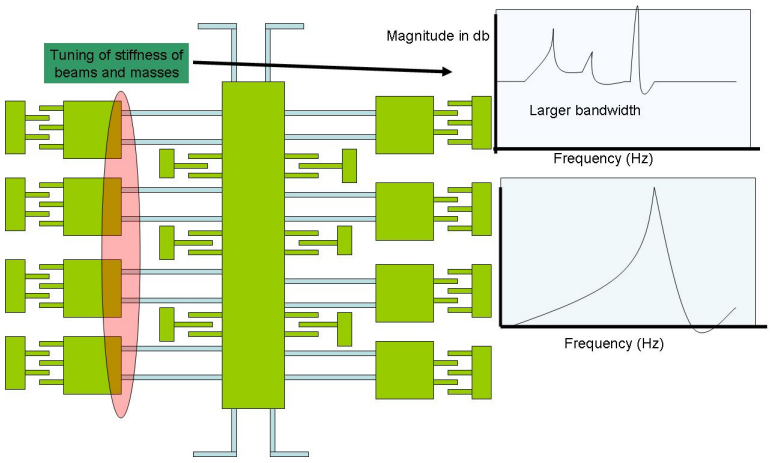

Figure 8.1: Array of Masses to Give a Very High Sensitivity or Large Bandwidth

of this type of design is the reduction in the cross coupling of different modes as each masses are totally decoupled from each other(experimental confirmation not done). The stiffness of the beams were verified by the pull in measurements and which gives the idea of tuning of

stiffness and masses which in turn the resonant frequency. A new noise analysis methodology was discussed and a novel noise based optimization of the gyroscope was described. This methodology was published in the conference paper[14] and the extension of noise based optimization of the gyroscope is submitted to a journal [15].

8.1 Future Work

This thesis lacks the design of the readout circuit which could be incorporated in the future. A semi-digital readout circuit involving IC555 timers can be made as seen in figure readout The inertia cluster of sensors is a big vision and a big project which would include, ac-

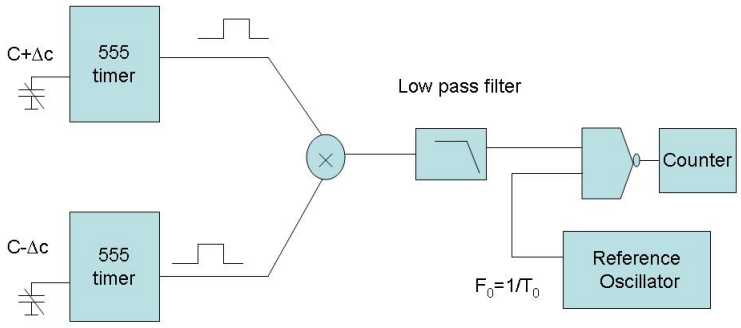

Figure 8.2: Readout Circuit

celerometers ,gyroscopes and a sound readout circuit. The design of the accelerometer and readout circuit is currently under research by the other group members of adaptive MEMS research lab.

Bibliography

[1]P. Greiff, B. Boxenhorn, T. King, and L. Niles. Silicon monolithic micromechanical gyroscope. Tech. Dig. 6th Int. Conf. Solid-State Sensors and Actuators (Transducers91), San Francisco, CA, June 1991, pp. 966-968.

[2]Cenk Acar."Robust Micromachined Vibratory Gyroscopes".(Ph.D.thesis),UC Irvine,Irvine,California,2004.

[3]Said Emre Alper, Kivanc Azgin, Tayfun Akin."A high-performance silicon-on-insulator MEMS gyroscope operating at atmospheric pressure".SensorsActuators A,vol.135,pp.3442,July 2007.

[4]http://www.melexis.com/html/pdf/Melexis2004.pdf.

[5]Ashwin.A.Seshia."Integrated Micromechanical Resonant Sensors for Inertial Measurement Systems". (Ph.D. thesis),UC Berkeley,Berkeley,California,2002.

[6]W.C. Young."Roark's Formulas for Stress and Strain". McGraw-Hill, Inc., pp.93-156, 1989.

[7]Sarne Hutcherson and Wenjing Ye, "On the squeeze film damping of micro-resonators in the free molecule regime", Journal of MEMS,14(2004)1726-1733.

[8]Minhang Bao,Heng Yang,"Squeeze film air damping in MEMS",Sensors and Actuators,A136(2007) 3-27.

[9]Luis Alexandre Rocha, Dynamics and Nonlinearities of the electromechanical coupling in inertial MEMS, (Ph.D.thesis),TU DELFT, Jan 2005.

[10]W.A. Clark, R.T. Howe, and R. Horowitz. "Surface Micromachined Z-Axis Vibratory Rate Gyroscope". Proceedings of Solid-State Sensor and Actuator Workshop,June 1994.

[11]N. Yazdi, F. Ayazi, and K. Najafi. "Micromachined Inertial Sensors". Proc. of IEEE, Vol. 86, No. 8, August 1998.

[12]N. Barbour, and G. Schmidt. Inertial Sensor Technology Trends. IEEE Sensors Journal, Vol. 1, No. 4, Dec 2001, pp. 332-339.

[13]http://www.memscap.com/mumps/documents/SOIMUMPs.dr.v4.pdf

[14]Mrigank Sharma, Akila Kannan, Edmond Cretu, "Noise-based Optimisation and Noise analysis for Resonant MEMS structures ", Proc. of DTIP 2008 (Symposium on Design, Test, Integration and Packaging of MEMS/MOEMS), Nice, France,9-11 April,2008.

[15] Mrigank Sharma and Edmond Cretu,"Extension of Noise-based Optimisation and Noise analysis for Resonant MEMS structures to the design and modeling of a gyroscope".Journal of Microsystem technologies (special edition DTIP 2008),submitted(2008).

[16]Edmond Cretu,"Inertial MEMS Devices Modeling,Design and Applications",(Ph.D.thesis),TU DELFT,October 2003.

[17] Timo Veijola, Analytical model for perforated squeeze-film dampers,Proceedings of DTIP 2006, Stressa, April 2006, pp 36- 41

[18] TimoVeijola et al, Simulation model for Micro-mechanical Angular rate sensor, Sensors and Actuators A 48,pp293-248,1995

[19]Sunil A. Bhave, Joseph I.et.al.,"AN INTEGRATED, VERTICAL-DRIVE, IN-PLANE-SENSE MICROGYROSCOPE",The 12th International Conference on Solid State Sensors, Actuators and Microsystems, Boston, June 8-12, 2003.

[20]www.melexis.com

[21]http://www.tanner.com/Labs/research/technologies/moics/opticalcomm.htm

[22]www.memagazine.org

[23] Yiyi Zeng,"Design of a MEMS-based optical accelerometer with large measurable range and high sensitivity",(M.A.Sc. thesis),UBC,Vancouver,Canada,April 2008.

[24]A Sharaf,et.al.,"Design and simulation of a new decoupled micro-machined gyroscope",Journal of Physiscs,34(2006),464-469

Part I

Appendices

Appendix A

First Appendix

A.1 Evolution In Surgery: From Open To Computer Assisted Via MIS

Many invited papers have covered this topic from the perspective of understanding the MEMS requirement in surgery. The paper [1] is one such paper which depicts the application of MEMS in Surgery. This paper also shows the various development of surgery from the open to minimal invasive. Surgery is the treatment of the disease or the other ailments through manual and instrumental means. The bodies in the past (not far) had to be cut open and the surgeon had the full contact of the organs . The tissues had to be cut and sewed manually ,this era began in 1867 with Lister's use of antiseptics in the operating room and was known as era of Open Surgery. The large incision on the patient allowed surgeons direct view and access of the organs and disease site. This ,however caused lot of pain to the patient and increased the recovery and healing time. The next era began in 1985, when Muhe performed the first laparoscopic cholecystectomy [2], or gall bladder removal surgery with a fibre optic scope, and the generation of surgical procedures was born. This advanced technique is commonly known as the MIS but also is termed as key hole, micro, telescopic ,less invasive and minimal access surgery. It is seen in [3] that the majority of the pain and trauma caused to the patient was due to the incision made by the surgeon to access the affected spot rather than the procedure itself. In [4] it was showed that the hospital stay was reduced by 59% and the patients recovered much faster.

A.2 Minimally Invasive Surgery

The endoscopic procedures and catheterization are the two famous examples of MIS. In the endoscopic procedure the doctor can control the tip of the endoscope through a flexible wire. To inject medicine into the blood vessel or measure the blood pressure , the catheterization is required. The catheter is of very small diameter and is required to be guided by the guide wires. The guide wires are manipulated manually by the doctor and when the exact location of the site is found, the catheter is introduced as seen in figure A.1.

Figure A.1: has been removed because of copyright restrictions. The information removed is catheter and Guide wire used in MIS from [5]

The catheter wire guide is usually removed when the location of the site is found. The positioning of the catheter is dependant on the skills of the doctor. In navigation of the catheter, doctors observe the position of the catheter tip by using the X-ray radioscopy and angiography [5]. The obtained information is usually insufficient as the acquired images are 2-D and don't show the information of the location of the tip of the catheter. This hampers the binocular vision eliminating the surgeon's depth perception. Usually a surgical assistant holds and maneuvers the endoscopic camera though most surgeons prefer holding themselves. The images from the camera are usually magnified and small motions such as the tremor in the surgical assistant's hand or even the small change in the body movement can cause surgical team motion induced nausea[1]. The surgeons also loses the freedom of movement as compared to open surgery. There is constraint in the instrument's motion [5] and is restricted to four degree of movement (in/out, left/right, up/down, and rotation). The trocars also act as pivot points and cause the surgical instruments to move in the opposite direction to the surgeon's hand. When the surgeon is moving to the left the tool moves to the right. This also gets amplified with also hinder the movement which make the process less smoother. To make things more difficult, there is no tactile feedback, so the surgeon has no sense the depth of the insertion of the tool. The seals and the valves can of how hard he is pulling, cutting ,twisting and suturing etc.

A.3 Computer Assisted Surgery

The third category of the surgery is the Computer Assisted Surgery, where the robots are used to help the surgeons. This aids in the feedback and the surgeon is guided at every instant. In the [1] ,surgical da vinci robotic system, the surgeon sits comfortably at a computer console instead of having to stand for long operations. The three armed robot takes its place over the patient and holds the endoscopes in one arm and other surgical tools in other hand. The figure A.2 and figure A.3 show the system and surgical stereo display system. Accuracy is improved by employing tremor cancelation algorithm to filter

Figure A.2: has been removed because of copyright restrictions. The information removed is Intuitive Surgical da Vinci Robotic System from [1]

Figure A.3: has been removed because of copyright restrictions. The information removed is Intuitive Surgical Stereo Display and Joysticks from [1]

surgeon's hand movements. Motion scaling improves accuracy by translating large ,natural movements into extremely precise movements. This can be shown in the [1] where the freedom of movement of hand is compared with the arm of a robot as seen in figure A.4.

Figure A.4: has been removed because of copyright restrictions. The information removed is Multi Degree of Freedom from [1]

In the paper [6] a novel image - guided system for precise automatic targeting in keyhole minimally invasive neurosurgery is discussed. The system consists of a miniature robot fitted with a mechanical guide for needle /probe insertion. It automatically positions itself with respect to predefined targets in a preoperative CT/MRI image following. This methodology depicts how feedback in this case magnetic feedback aids in surgery and is seen in figure A.5.

Figure A.5: has been removed because of copyright restrictions. The information removed is MARS Robot Clamped on Skull from [6]

Figure A.6: has been removed because of copyright restrictions. The information removed is Feedback Obtained by Magnetic Resonation [6]

The movements of the MARS robot is guided by the 3-D feedback provided by the magnetic resonance. The figure A.6 shows the feedback obtained on the computer. There are many different ways of getting the feedback and of sensing the movement of the tools. Navigation and 3-D positioning can be achieved by the micro-system sensors like accelerometers and gyroscopes. Accelrometers are used for linear sensing and the gyroscopes for the rotational sensing. By including associated electronics with the mems structure 3-D feed back can be achieved. No one has yet approached using mems sensors like accelerometers and gyroscopes for the navigation.

A.4 Navigation Systems, Sensors And Actuators

The previous section highlighted the shortcoming of the keyhole surgery. The vision of the surgeon is 2-D and not 3-D this hampers hand-eye co-ordination. For safe manipulation of tools like catheter in blood vessels, real time information about the position and the orientation is important. Generally, x-ray radioscopy and angioscopy using a contrast medium are used to observe the position. Prolonged X-ray usage is harmful and wearing of special shield is essential for doctors. Ultrasounding imaging is also used for positioning of catheter using lead zicornate titanate in the tip for the ultrasound sensing[21]. MRI provides large opportunity and are being implemented too. The issues with MRI sensing is cost. In MRI coil is wounded on the catheter. These windings have certain turns and certain angles to

get magnetically activated externally. They are externally excited and the coils get charged with different signals and orient the catheter accordingly. The magnetic sensor system for monitoring position and orientation of catheter tip is shown in figure A.7.

Figure A.7: has been removed because of copyright restrictions. The information removed is Magnetic Sensor System for Monitoring Position [5]

The coil would on the catheter is usually filled with Gd-DTPA doped water, twisted wire or a microcoil with electronic lead wires placed at the tip of the catheter winding for the tracking using MRI as seen in figure A.8. In the [5] there is discussion over the

Figure A.8: has been removed because of copyright restrictions. The information removed is Windings on Catheter for Tracking Using MRI [5]

integration of magnetic navigation system with a 3-D map of the internal body acquired by using helical computed tomography. There is also description of fixation of magnetic field transmitters at the tip of the catheter. as shown in figure A.9 Figure A.9 has been removed because of copyright restrictions. The information removed is Magneto-Impedance Effect Sensor Attached on Tip of Catheter[5]

Figure A.9: has been removed because of copyright restrictions. The information removed is Magneto-Impedance Effect Sensor Attached on Tip of Catheter[5]

A.5 Actuators Used In Steering For Navigation

In [5] ,actuators for navigation of tools are widely discussed. Endoscopes are usually flexible and can be bent. Not always the blood vessel will be ideal and there may be loops which may require the catheter move snake-like. The [5] shows the bending, torsional and extending active catheter using SMA coil . SMA coil is made up of TiNi and contracts when heated above a certain transition temperature as seen in figure A.10.

The current is varied in the coils which are made up of lead wires to produce the desired motion. The problem with this is that many wires are required for actuator. The paper [7] discusses on how the wiring can be reduced.

The discussions in section 3 were related to navigation of tools . Literature survey , showed that there were many articles on navigation of tools after they were attached to the

Figure A.10: has been removed because of copyright restrictions. The information removed is Bending and Extending Active Catheter Using SMA Coil Actuator [5]

spot in the body for observation. However, while introducing the endoscope through a small hole constant manipulation both linear and rotational is required. To get the exact location ,surgeons require constant feedback for the slightest movement they make. MRI, ultrasound techniques were discussed in the previous sections and were found to give only 2-D movement . The Robotic or Computer assisted surgery was discussed to reduce the error caused by the surgeons due to tremor in hand. This motivates us to look into the other alternatives with 3-d feedback for the surgeons to make easy navigation. A novel methodology is proposed in this paper using mems structures like gyroscopes and accelerometers for sensing the co-ordinates of the tool . Accelerometers are used to sense the linear displacements and gyroscopes the rotational displacement.

A.6 Navigation Methodology Using Inertial Sensors

The block diagram 1.2depicts that there is a software in which the movement of tool is predefined in terms of co-ordinates. When the tool like catheter is actually inserted in the body through a keyhole, its movement is mapped continuously with the co-ordinates of the software. The minimal inertial sensors both accelerometers and gyroscopes are used for linear and rotational movement. Electronic read out can be made used where the movement and the rotation of the sensors is translated into voltages and currents. Both these structures have interdigated plates acting like capacitors. These capacitors vary with the linear motion in case of accelerometer and with the rotational motion in gyroscopes ,thus varying the distance between the interdigated plates. The net capacitances can be evaluated and so the voltages associated too. These readouts may take larger delays and there may be issues related with the biocompatibility of the electronics packaging with the tool. Researchers also suggest optical readout mechanism where the laser is thrown into the accelerometer and the gyroscopes. The distance between the interdigated plates when changed will cause the laser to get deflected. Another undeflected laser is kept for reference and is used to measure the changes caused in the laser due to inertial mass sensors.

A.7 Biocompability Issues For MEMS Structures

MEMS structures when used in biomedical applications have to be biocompatible. The MEMS structure in contact with the body (blood vessel, tissue etc.) should not affect the biological environment, similarly the later should not affect the functioning of the prior. MEMS structures can be used either as in vivo or as in vitro. Material which make MEMS structure should be selected based on the basis of chemical, toxicological, physical, electrical, morphological and mechanical properties most suitable to the task [14]. The type of contact

and duration are factors to be considered. Some of the MEMS structures are required to be permanently attached to the body like pacemaker and some are for lesser time like pressure sensors. Frequency of use is given as acute, sub acute and chronic [14] and pacemaker for instance falling in the chronic category.

The gyroscopes and accelerometer have to be attached with the tools and will be used in vivo applications. However, the vast assortment of MEMS component and other structures like cantilever, rotors, micropumps etc have been checked and tested mainly for the in vitro applications only . The biocompatibility of the MEMS structures which are used both in vivo and in vitro applications can be improved through micro fabrication technology. The [15] [16] [17] discuss various micro fabrication technology from packaging to coating and bonding methodologies. In [15] it is stated that issues of biocompatibility occur at the interface between device and tissue or blood, which affirms that the packaging of biosensor is essential for the success of any sensor design. In the case of the tools which are made up of steel and have sensors like gyroscopes and accelerometers in the tip can be coated with titanium -nitride-oxide alloys via physical vapor deposition in an effort to improve the biocompatibility . The biosensors usually fail due to the protein adsorption and cellular adhesion , as well as the fibrous capsule formation which have led to failure in vivo sensors ,limiting and or suppressing the measured signal in a temporal fashion, so these coatings like titanium-nitride- oxide alloy as mentioned above has helped. The ISO 10993 standards [14] [15] have outlined minimum tests for material characterization ,toxicity and biodegradation that may be augmented depending on the actual device usage. Biocompatibility can be assessed in many ways. In vitro assays include leaching of material, corrosion testing, protein adsorption testing and etc. In the case of in vivo biocompatibility issues, it is noted that the size, shape and surface structures will also define the variation in the biocompatibility [15].

The silicon substrates are the basis of gyroscopes which are used in this paper. Many papers have discussed the compatibility issues of the silicon. In [15][16] showed that the silicon nitride and SU-8 leached detectable non volatile residues in aqueous physiochemical tests and only SU-8 leached detectable non volatile residues in iso-propyl alcohol. These results show that there are lesser concerns about using these materials in vivo applications.

Analytical bio-MEMS usually have many units integrated on the same platform. In our case wave guides, MEMS structures (gyroscope), catheter and associated electronics. The degree of integration (monolithic, hybrid, discrete subsystems) and to make the in disposable and durable subsystems. There is also another option where in a decision has to be taken for using biocompatible packaging methods or to encapsulate conventionally parts of bio-MEMS with a biocompatible material. An example shown in [packaging] wedge - wedge wire bonding and ball wedge bonding is compared and is shown that bio molecules cannot tolerate the high temperature which is used in ball-wedge bonding. Micro assembly processes like precise positioning, orientation , joining and assembling techniques also define the integration of many components on the same platform. The lack of flexibilities and adaptability of most current assembling systems known from non bio- MEMS which are often made up of silicon to other kinds of material and processes including the joining technologies. Many papers have explored for the usage of new material and processing techniques. Polymers like bio-erodible polymers have been discussed [18][16]. In [15] it is

showed that protein adsorption and bio fouling are the reasons why different polymers are explored. In [17] it is stated that protein adsorption an cellular adhesion , as well as the fibrous capsule formation have been identified as leading cause of in vivo sensor failure. Surface immobilized polymers seem to be the best option where poly ethylene glycol (PEG) is applied which reduces both bio fouling and protein adsorption. The figure A.11 shows the diagram of bio-fouling while using the catheter on the patient. The other polymers under

Figure A.11: has been removed because of copyright restrictions. The information removed is Bio-fouling in Using Catheter [5]

research which are showing good protein inhibition proteins are tetraglyme , copolymer of ethylene glycol such as poly(acrylamide-co-ethylene glycol and poly (L-lysine) grafted with PEG side chains. There is also research on SAM (Surface Assembled Monolayer) have been known for more than a decade to passivate surfaces against protein and cellular adsorption .These mono layers spontaneously form dense over layers on surfaces related to MEMS. The first type of SAMs resistant to adsorption have been identified as ethylene glycol and large range of terminally functionalized alkanethiols has been found to be protein resistant.

Appendix B

Second Appendix

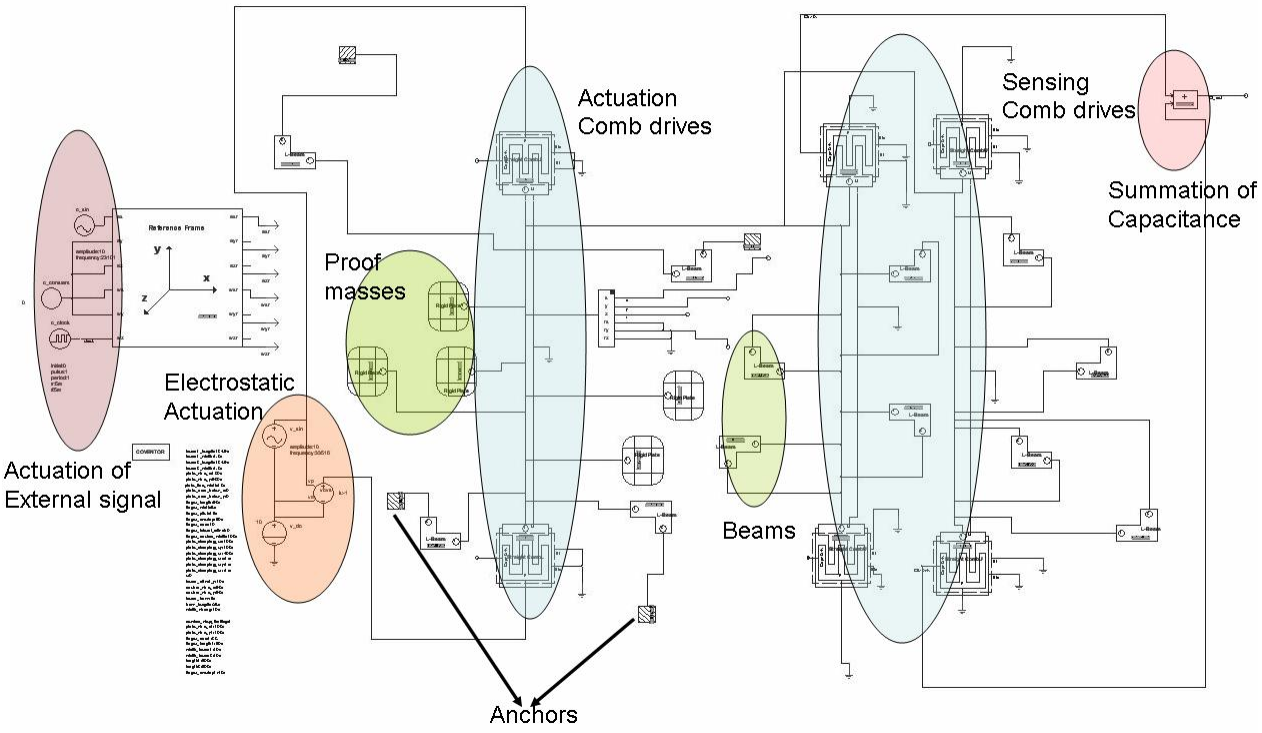

Figure B.1: Saber Macromodel of a Gyroscope System

Mrigank Sharma was born in 1984 in Lucknow, North India which is also known as "City of Nawabs". Mrigank grew up in Ankleshwar (Gujrat)first 9 years of his life and then in the beautiful city of Chennai (Madras)in Southern India for 13 years. He got his Bachelor of Engineering in Electronics and Communication Engineering with first class and distinction from Sri Siva Subramaniya Nadar College of Engineering (Anna University) in 2006. During his third and final years of engineering he was an undergraduate Research Trainee at WAran Research FoundaTion(www.warftindia.org),where he performed research in Marconi group (CAD for VLSI)under the supervision of Professor.N.Venkateswaran. Since 2006 he has been performing research under the supervision of Edmond Cretu in the field of MEMS

Publication (Journal Submitted)

[1]Mrigank Sharma and Edmond Cretu,"Extension of Noise model and noise based optimization of resonant MEMS structures to the design of a gyroscope", JOURNAL OF MICROSYSTEM TECHNOLOGIES, issue DTIP 2008,06/2008.

Publication (Conferences and Workshops)

[1]Mrigank Sharma, Akila Kannan, Edmond Cretu, "Noise-based Optimisation and Noise analysis for Resonant MEMS structures ", DTIP 2008 (Symposium on Design, Test, Integration and Packaging of MEMS/MOEMS), Nice, France,9-11/Apr/2008.

[2]Mrigank Sharma, N.Venkateswaran, Krishna Bharath, Murari Mani,"Digital Model for Interconnect Analysis",IEEE CAS NORCHIP 2005, Finland, IEEE CAS, 11/2005.

[3]Mrigank Sharma, N.Vekateswaran, R.Karthik, Abhishek Gopal, N.R.Arun, "Analysis of Crosstalk Masking of Electromigration and On–Chip Tracking of Interconnect Aging",

IEEE 14th North Atlantic Test Workshop, Vermont,USA, IEEE, 05/2005.

Publication(Thesis and White Papers)

[1]Mrigank Sharma, "Non uniform ground plane modeling and clock distribution in 2-d IC's",(Thesis) Marconi(Mixed Signal group), 2006.

[2]Mrigank Sharma, N.Venkateswaran,"Interconnect Length Prediction For MIP S.C.O.C: Part I Memory In Processor Super Computer on a Chip (MIP S.C.O.C) White paper.", Waran Research Foundation (www.warftindia.org), Chennai, India, 2006.

[3]Mrigank Sharma , et.al,"Low Power FPGA Architecture and Mapping Techniques".Finalyear Engineering Project,Submitted to Anna University.Grade-(198/200).

Technical Talks

[1] Abhishek Gopal and Mrigank Sharma"Power and Signal Integrity Issues",Dhi Yantra 06',Workshop on Brain Modeling and Supercomputing ,Chennai, India.

[2]Mrigank Sharma,"Interconnect Issues"Dhi Yantra 06',Workshop on Brain Modeling and Supercomputing,Chennai,India.

Bibliography

[1] Keith J. REBELLO, "Application of MEMS in Surgery," Proceeding of the IEEE, Vol.92. No.1, January 2004

[2] W. Reynolds Jr., "The first laparoscopic cholecystectomy," J. Soc. Laparoendoscopic Surg., vol. 5, pp. 89-94, 2001.

[3] J. A. Lujan, P. Parrilla, R. Robles, P. Marin, J. A. Torralba, and J.Garcia-Ayllon, "Laparoscopic cholecystectomy vs open ..," Arch. Surg., vol.133, pp. 173- 175, 1998.

[4] Yoishi Haga et.al, "Biomedical microsystem for minimally invasive diagnosis and treatment", Proceedings of the IEEE, Vol 92, no.1, January 2004

[5] T. Katsumata, Y. Haga, K. Minami, and M. Esashi, "Micromachined 125m Diameter Ultra Miniature Fiber-Optic Pressure Sensor for Catheter," Trans. IEE Jpn. vol. 120-E, pp. 58-63, 2000.

[6] Ruby Shamir et.al , " An augmented reality guidance probe and method for image-guided surgical navigation ," 5th International Symposium on Robotics and Automation 2006, Sam Miguel Regala Hidalgo, Mexico ,August 25-28 ,2006.

[7] K. Park, K. Minami, and M. Esashi, "An integrated communication and control system for a multi-link active catheter," J. Micromech. Microeng., vol. 6, pp. 345-351, 1996.

[8] Rijk Edwin Oosterbroek, "Modeling, Design and Realization of Microfluidic components," Thesis volgens besluit van het College voor Promoties

[14] Steven S. Saliterman, "BioMEMS and Medical Micro devices", SPIE Press Monograph series Vol.no PM153

[15] Amy C.Richards et.al, "A Bio MEMS Review: MEMS technology for physiologically Integrated Devices," Proceedings of the IEEE, Vol .92, NO.1, January 2004

[16] Thomas Velten ET. Al, "Packaging of Bio- MEMS: Strategies, Technologies, and Applications," IEEE transaction on advanced packaging, Vol.28, No4. November 2005.

[17] Gabriela Voskerician et. al, " Electrochemical Characterization and In Vivo Biocompatibility of a thick -Film Printed Sensor for Continuous In Vivo Monitoring," IEEE SENSORS JOURNAL ,Vol .5,No.6,December 2005.

[18] L.A. Ferrara et.al, "An in vivo Biocompatibility assessment of MEMS material for spinal fusion monitoring," Biomedical Microdevices 5:4, 297- 302, 2003.

[19] William A Rutula, New Disinfection and Sterilization Methodologies, Vol 7, No.2 March 2002.

[20] T. Katsumata, Y. Haga, K. Minami, and M. Esashi, "Micromachined 125μm Diameter Ultra Miniature Fiber-Optic Pressure Sensor for Catheter," Trans. IEE Jpn., vol. 120-E, pp. 58-63, 2000.

[21] D. Vilkomerson, B. Gardineer, and H. Hojeibane, "Quasiomnidirectional transducers for ultrasonic electronic-beacon guidance of invasive devices," in SPIE, vol. 1733, 1992, pp. 154-165.